REPORT DOCUMENTATION PAGE

Form Approved
OMB No. 0704-0188

1. AGENCY USE ONLY (Leave Blank)	2. REPORT DATE	3. REPORT TYPE AND DATES COVERED
	9/30/2005	SBIR Phase I Final Report 02/01/05 - 08/01/05

4. TITLE AND SUBTITLE
Ground Shock Propagation in Spatially Random Geological Media

5. FUNDING NUMBERS
HDTRA1-05-P-0026

6. AUTHOR(S)
F. Wong, J.. Mould, and V. Pereyra

7. PERFORMING ORGANIZATION NAME(S) AND ADDRESS(ES)
Weidlinger Associates Inc.
4410 El Camino Real #110
Los Altos, CA 94022

8. PERFORMING ORGANIZATION REPORT NUMBER

9. SPONSORING/MONITORING AGENCY NAME(S) AND ADDRESS(ES)
DTRA/TDTTP
1680 Texas St. SE
Kirtland AFB, NM 87117

10. SPONSORING/MONITORING AGENCY REPORT NUMBER

11. SUPPLEMENTARY NOTES

12a. DISTRIBUTION/AVAILABILITY STATEMENT
Approved for public release; distribution unlimited.

12b. DISTRIBUTION CODE

13. ABSTRACT (Maximum 200 words)

Report developed under SBIR contract for topic HDTRA1-05-P-0026. The main issue being addressed is as follows: Given what is known about a rock site, what can one say about the uncertainty in the ground-shock environment that can be expected from an explosive event? To be sure, the amount of data available is directly connected with the ground-shock uncertainty. But does a quantitative, rational procedure exist that one can use to estimate the environment uncertainty associated to the degree of uncertainty on the site?

We have demonstrated in this project: (1) How heterogeneity and spatial variability of rock properties at a site, as evidenced by state-of-the-art measurements taken at the demonstration site, are captured as random fields using geostatistical techniques; (2) How these fields of mostly low-stress, in-situ or laboratory properties, which are representative of the kinds of measurements being taken, could be used to infer rock-mass mechanical properties in the high-stress, high-strain-rate response regimes of interest; (3) How the rock-mass property fields were used in ground-shock simulations to generate the corresponding ground-shock fields, employing stochastic finite-element techniques; and, lastly, (4) How local variability in the simulated ground-shock environments could be readily elicited from the stochastic realizations.

14. SUBJECT TERMS	15. NUMBER OF PAGES
SBIR Report	37
	16. PRICE CODE

17. SECURITY CLASSIFICATION OF REPORT	18. SECURITY CLASSIFICATION OF THIS PAGE	19. SECURITY CLASSIFICATION OF ABSTRACT	20. LIMITATION OF ABSTRACT
Unclassified	Unclassified	Unclassified	

FINAL REPORT

Contract HDTRA1-05-P-0026, CDRL A001

Ground Shock Propagation in Spatially Random Geological Media

September 30, 2005

Submitted to:

Dr. Robert Reinke
DTRA/TDTTP
1680 Texas St. SE
Kirtland AFB, NM 87117
(505) 846-5847
robert.reinke@abq.dtra.mil

Submitted by:

Weidlinger Associates, Inc.
4410 El Camino Real, Suite 110
Los Altos, CA 94022

EXECUTIVE SUMMARY

The main issue being addressed is as follows: Given what is known and not known about a rock site, what can one say about the uncertainty in the ground-shock environment that can be expected from an explosive event? To be sure, the less (more) data we have on a site, the greater (smaller) the ground-shock uncertainty. But does a quantitative, rational procedure exist that one can use to estimate the environment uncertainty that corresponds to the degree of uncertainty on the site?

As mentioned in our proposal, there are four subsidiary issues: (1) Characterization and quantification of the variability in the mechanical properties of a rock site - how can the variability be best encapsulated in a stochastic model? (2) The prediction of the ground-shock response for the stochastic prescription - is the state-of-the-art in stochastic finite-element technology adequate for this purpose? (3) Extraction of the local and spatial uncertainties in the predicted ground-shock environment – given stochastic realizations of the ground shock environment, how can their local and spatial uncertainties be encapsulated? And, most importantly, (4) the ultimate goal of attributing these uncertainties to the site uncertainties – how can a quantitative, site-environment uncertainties transfer-function be established?

Such a transfer function can be invaluable. Site databases vary from application to application and have various degrees of incompleteness; those commonly encountered in real-world situations are usually quite sparse. The ability to quantify the environment uncertainty based on the uncertain site data will facilitate field-test planning, structural vulnerability assessment, data collection, and other goals.

Note that site categorization for the purpose of assessing *explosive effects* is much more demanding when compared with, say, seismic profiling. The main reason is that the explosive phenomenology involves high stresses and high strain rates and, hence, mechanical properties of the rock-mass under these extreme conditions. Yet these properties cannot be measured directly and *insitu* at present; they can only be inferred from other measurements. Material behavior under said conditions is highly non-linear; thus the effects of heterogeneities and spatial variations inherent in geological materials become much more important. Hence, domains that can normally be considered uniform and homogeneous for seismic purposes do not behave as such when subjected to explosive effects.

We have demonstrated in this project: (1) How heterogeneity and spatial variability of rock properties at a site, as evidenced by state-of-the-art measurements taken at the demonstration site, could be captured as random fields using geostatistical techniques; (2) How these fields of mostly low-stress, in-situ or laboratory properties, which are representative of the kinds of measurements being taken, could be used to infer rock-mass mechanical properties in the high-stress, high-strain-rate response regimes of interest; (3) How the rock-mass property fields were used in ground-shock simulations to generate the corresponding ground-shock fields, employing stochastic finite-element

techniques; and, lastly, (4) How local variability in the simulated ground-shock environments could be readily elicited from the stochastic realizations.

Local variability addresses the question: What uncertainty could one reasonably expect in the ground-shock measurements at a location at the site in an explosive test. The figure below compares two cutout views of the volume of interest. They give the (mean ± 1σ) bounds on the distribution of the peak pressure, in MPa, where mean is the mean value and σ the standard deviation, respectively, of the 20 realizations obtained by finite-element simulation based on stochastic modeling of the site. As can be seen from the figure, the mean and σ values vary with location. At a given location, the (mean ± 1σ) bounds measure the variability that can be expected for that location and, hence, the local variability.

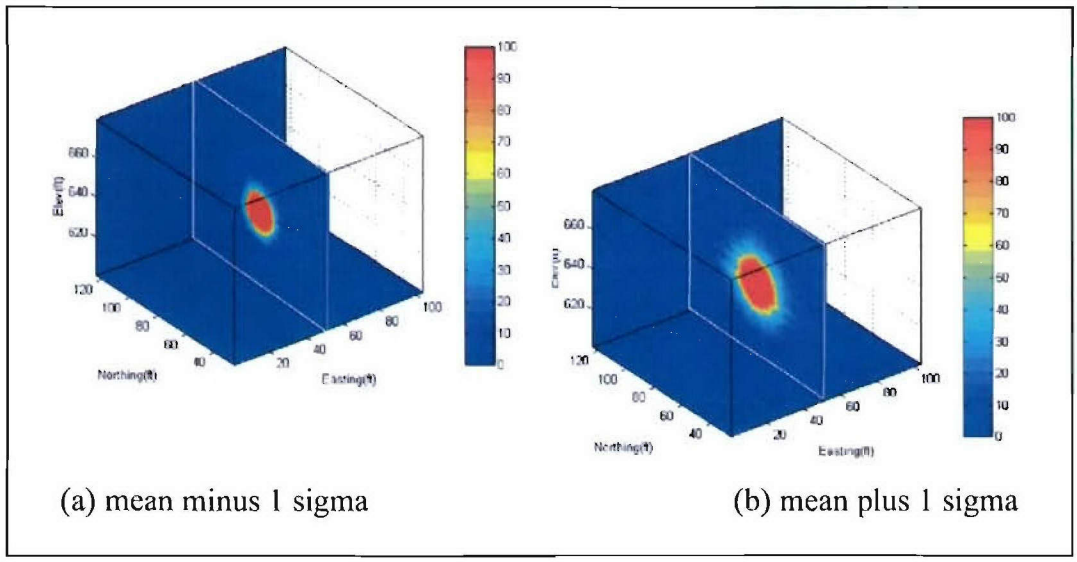

(a) mean minus 1 sigma (b) mean plus 1 sigma

On the other hand, we have yet to demonstrate how *spatial variability* exhibited in the same simulated environments could be encapsulated. Spatial variability addresses the question: How much variation in the measurement could one reasonably expect if it is made in a slightly different location. A relation between spatial site-property variability on the one hand and spatial ground-shock response variability on the other, has not been established[1].

[1] It is posited that the very same geostatistical models used to capture site-property variability may be applied to summarize environment variability. After all, realizations of the environment may be considered "response measurements" -- measurements that are made for all locations of the site as opposed to finite locations in site exploration. Hence, a relation between the geostatistical models of the site and those of the "response measurement", may be established.

DEMONSTRATION DETAILS

The demonstration was carried out using the Mitchell Quarry (MQ) test bed that evolved from a recent site exploration project sponsored by DTRA to assess weapons effects on underground facilities. The MQ database is noteworthy not only for its diversity and comprehensiveness, which are unmatched, but also for the inclusion of RPSS soundings at over 30 locations of the site. While still sparse by geostatistics standards, these soundings, when supplemented by other data in the database, supported the characterization of a spatial variability model for the site – and constituted a key step in our demonstration.

Encapsulate Material Inhomogeneity and Spatial Variability Exhibited by the Site Database

It is common knowledge that site measurements are difficult to interpret at *face value* due to inherent material heterogeneity, spatial variations and measurement uncertainties. For example, the C_p ratio (ratio of *insitu* p-wavespeed to laboratory p-wavespeed, *squared*) of samples taken from the four boreholes at the site is given in Figure 1. Holes C2, C3 and C4, in particular, are in close proximity to one another, and if one assumes that the site consists mainly of uniform, horizontal layers, readings at these boreholes taken at the same elevation (i.e., for the same geological layer) should be highly correlated. However, the results presented in Figure 2 indicate otherwise. In fact, the correlation among boreholes C2, C3 and C4, which are very close to one another, is no better than the correlation between these holes, taken in turn, and hole C1, which is much farther away from the group (see Figure 1).

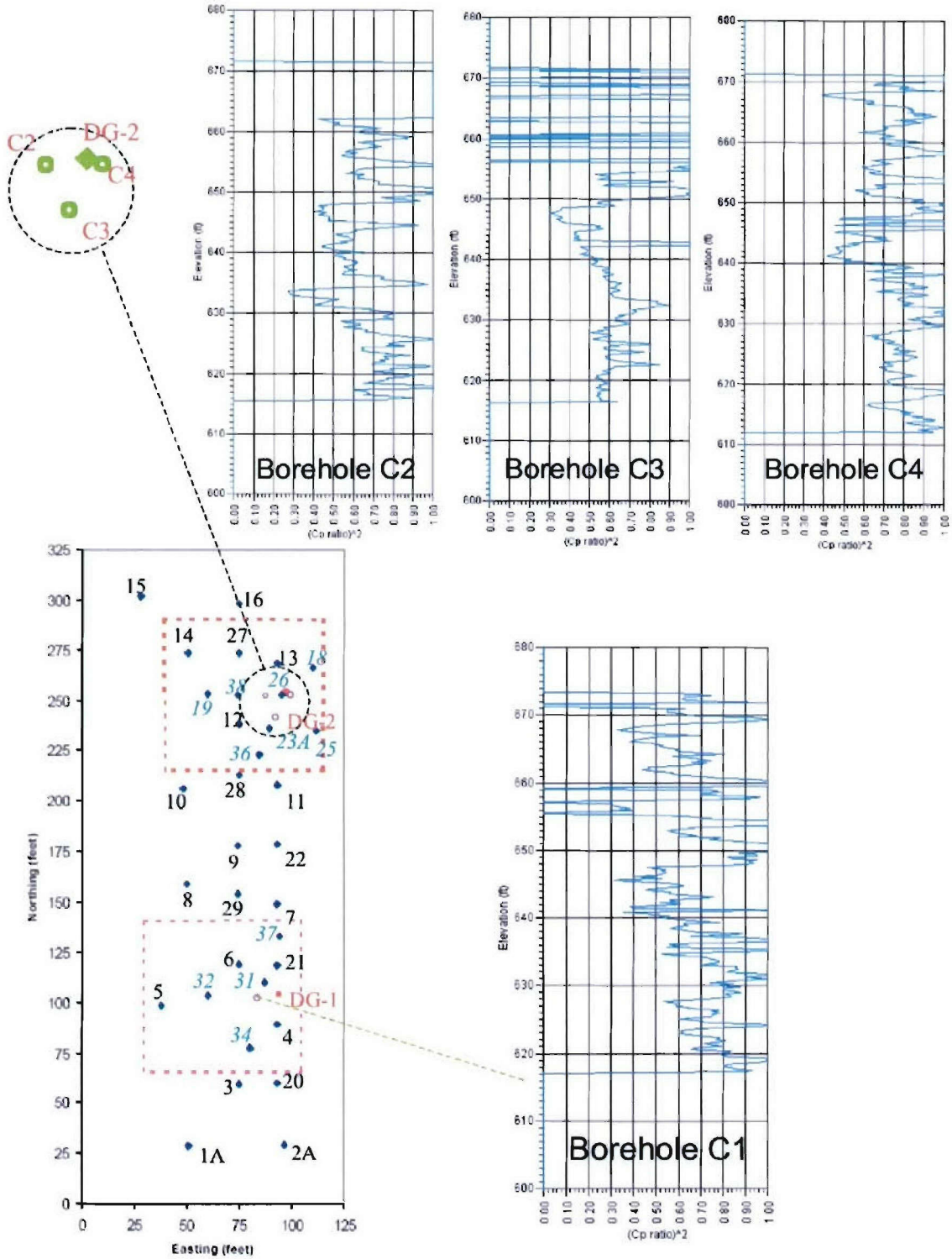

Figure 1. *Cp* ratio for samples in boreholes C1-C4, plotted versus elevation (ordinate).

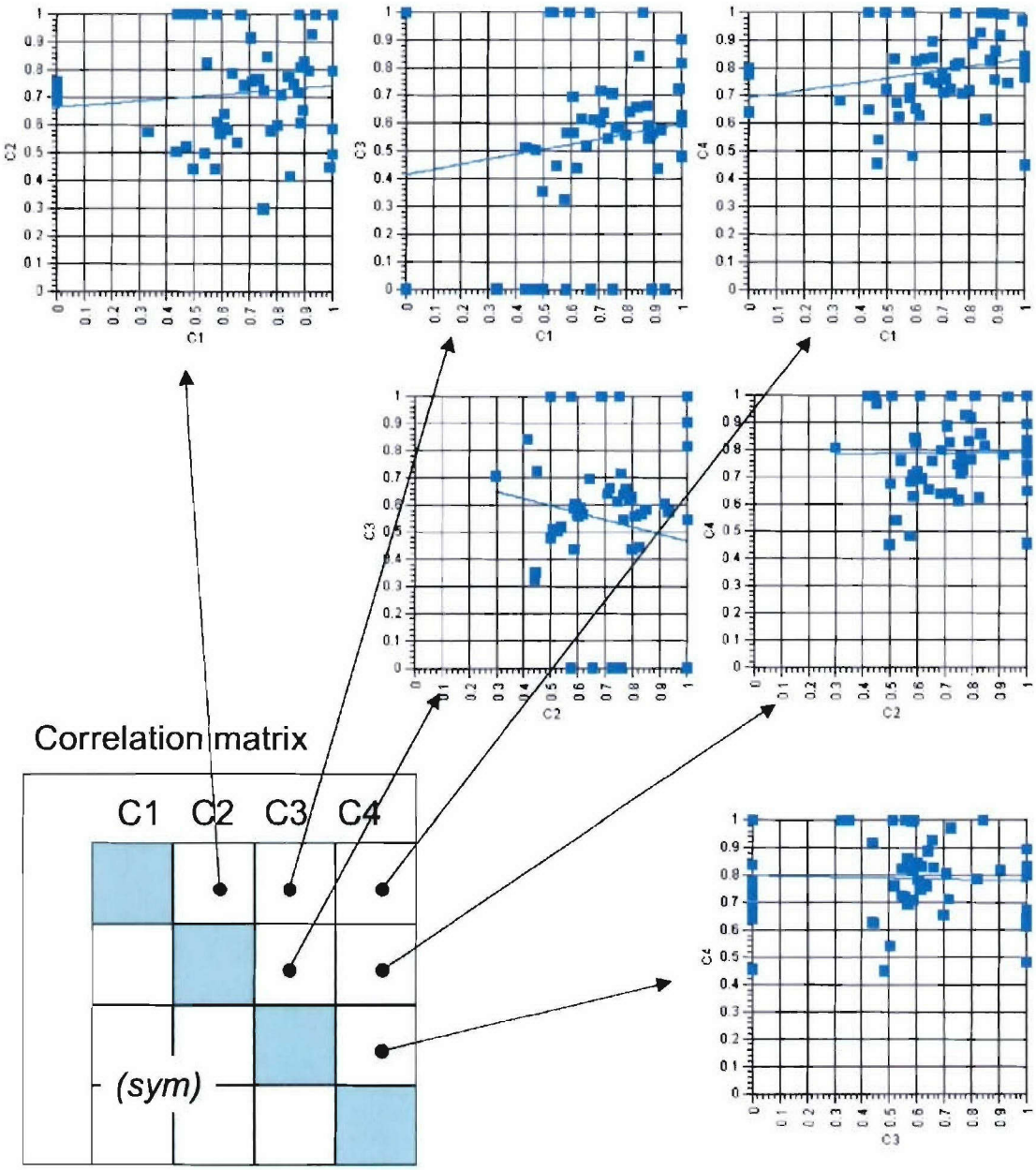

Figure 2. Correlation of *Cp* ratios taken from the boreholes C1 through C4; correlation is computed for samples that have the same elevation.

In this project, we found that the macro-structure of what appear to be random, spatial fluctuations (Figures 1 and 2), could be uncovered using geostatistical models. The key variable is spatial correlation, i.e., the correlation of material properties between two

points located some distance h apart; note that these two points do not have to be at the same elevation, as in Figure 2. Spatial correlation is expressed in the form of a variogram, which is a plot of the degree of variability (lack of correlation) as a function of the separation distance, usually in a given, fixed direction in three-dimensional space. Properties for points close together are expected to have high correlation (low variation) and those far apart are expected to have low correlation (high variation). The innovation introduced by geostatistics or variograms is that instead of looking at the relationship exhibited by a pair of points, one pair at a time, which can be baffling as we have seen in Figures 1 and 2, a variogram collects as many qualifying pairs as exist in the database, and takes the average of these pairs to enforce the relationship. In this way the macro structure of the underlying dependency is uncovered.

For example, the variogram for the same borehole data shown in Figure 1 is presented in Figure 3. As is generally the case, correlation (variation) depends not only on the separation distance, but also the orientation of the connecting line, i.e., pairs with the same separation distance h, but oriented in different directions, will in general exhibit different correlations. The results shown in Figure 3 indicate that two major orientations distinguish themselves: The horizontal and vertical directions, lending support to a basically horizontal layering site structure. Since the data points are more heavily populated in the vertical direction than in the horizontal direction (many more samples taken along the bore hole than there are boreholes), the vertical component of the variogram in Figure 3 is much better defined than the horizontal component.

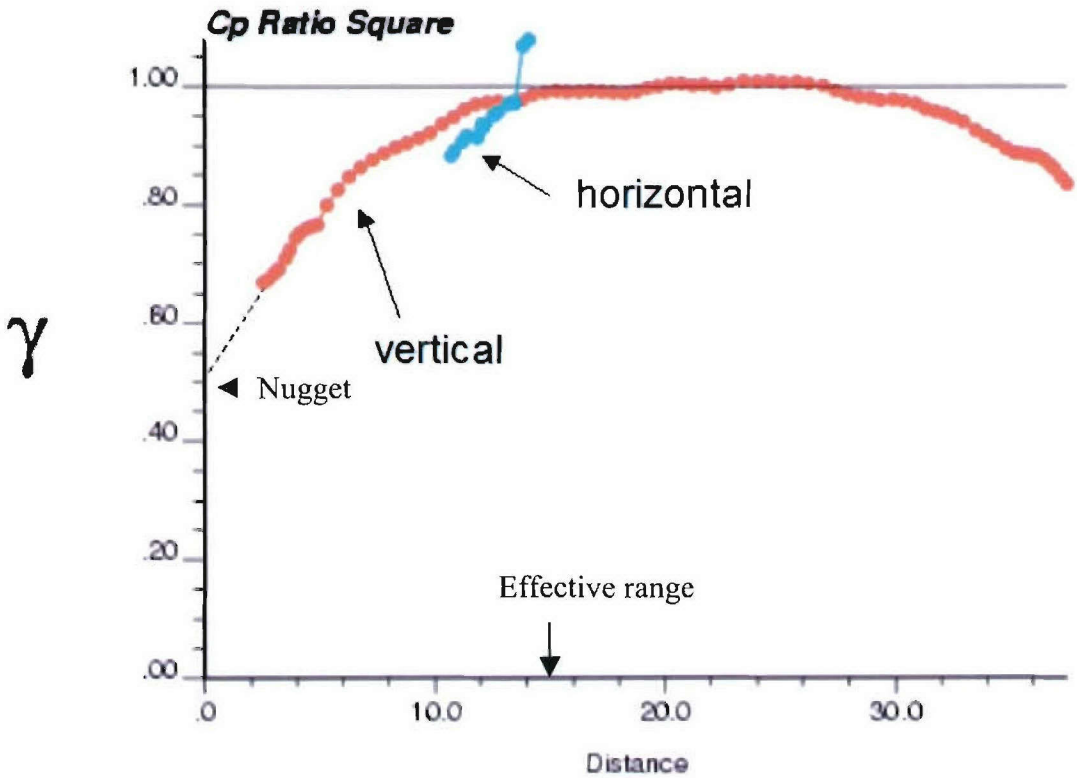

Figure 3. Variogram of *Cp* ratio, based on borehole data C1 through C4.

Two quantities in a variogram are of special interest: The asymptote and intercept. With reference to the vertical component of the variogram shown in Figure 3, the asymptote is reached at a separation distance of about 15 ft. Therefore, properties for points that are 15 ft or more apart *vertically* no longer correlate; they vary independently. For this reason, this distance is called the effective range. In this particular example, the borehole data used to generate the figure are sampled every 3 ft in elevation, so variogram information for separation distances 3 ft or less is lacking. Hence, the intercept (variogram value for separation distance = 0) can only be estimated by extrapolation of the curve, as indicated by the dash line in the figure; it is approximately 0.5, or 50% of the total variance (the asymptote). Reducing the sampling distance will yield more data to better support the intercept, but if we take Figure 3 at face value, the result implies a rather large component of inherent "noise" in the measurement. For this reason, the intercept is also called the "nugget" effect - random impurities in a mined nugget

For most practical purposes, the three parameters: Intercept (nugget), asymptote and effective range, define the variogram and, hence, the macro-structure of the spatial variability at a site. It is helpful to remember the analogy between the variogram, for spatial variability, and the density function for random numbers. While each random number (properties at a location) appears to have little overt relation to the next (properties at a different location), the samples (properties at site locations) are actually governed by a structure or model called density function (variogram). While variograms (density functions) are usually derived from data, as indicated herein, they are sometimes postulated or assumed as needed, e.g., when data are not available. The important point is, once postulated, the variogram (density function) dictates the site variability (random number sequence). Or, put differently, slightly different variograms (density functions) will lead to slightly different site variability profiles (random sequences).

The definition of the variogram (macro-structure of site variability) improves when the spatial database grows. In particular, we found that the RPSS index dataset, λp, covering 33 locations (Figure 4) gives rise to a much better defined structure than the four boreholes, as shown in Figures 5 and Figure 6 for the vertical and horizontal components of the variogram, respectively. These empirical results could be further consolidated into a model, given in Figure 7. This model then defines the structure of spatial variations of properties at the site as reflected in the RPSS dataset. We call it the vmodel, for variogram model, to distinguish it from the variograms themselves which are based on site data.

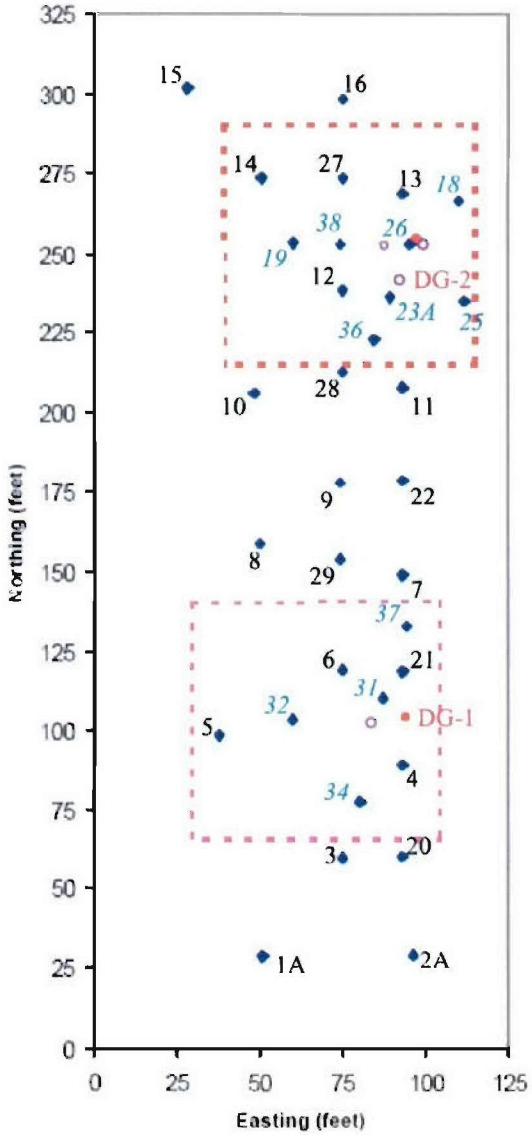

23 Phase 1 RPSS locations

Sounding ID	Local X Coordinate (ft)	Local Y Coordinate (ft)
DG-S1A	50.19	29.49
DG-S2A	96.03	29.95
DG-S3	75.00	60.00
DG-S4	93.00	90.00
DG-S5	36.00	100.00
DG-S6	75.00	120.00
DG-S7	93.00	150.00
DG-S8	50.00	160.00
DG-S9	75.00	180.00
DG-S10	48.00	208.00
DG-S11	93.00	210.00
DG-S12	75.00	240.00
DG-S13	93.00	270.00
DG-S14	50.00	275.00
DG-S15	19.00	300.00
DG-S16	75.00	300.00
DG-S20	93.00	60.00
DG-S21	93.00	120.00
DG-S22	93.00	180.00
DG-S23	93.00	240.00
DG-S27	75.00	275.00
DG-S28	75.00	215.00
DG-S29	75.00	155.00

(17,18,19,24,25,26 skipped;
29 – 6 = 23 pts)

11 Phase 2 RPSS locations

Sounding ID	Local X Coordinate (ft)	Local Y Coordinate (ft)
DG-S18	110.00	266.23
DG-S19	60.03	253.28
DG-S23A	89.00	236.00
DG-S25	~~11.88~~ 111.88	235.03
DG-S26	95.36	253.00
DG-S31	87.47	110.07
DG-S32	60.09	103.32
DG-S34	80.10	76.98
DG-S36	84.76	222.94
DG-S37	94.20	132.42
DG-S38	74.71	253.05

(total: 17,24,30,33,35 skipped;
23A replaces 23;
38 – 5 = 33 pts)

Figure 4. The RPSS dataset, with soundings at 33 locations, covers a much larger domain than the four boreholes.

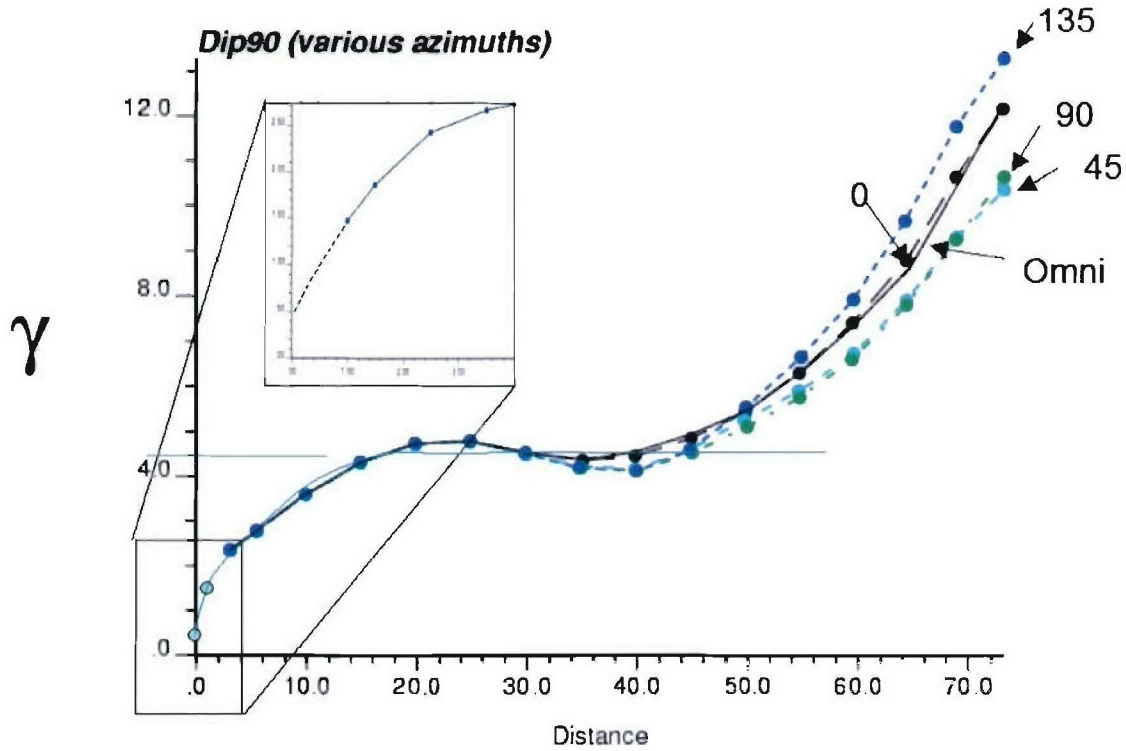

Figure 5. Variogram structure for RPSS index, λp; vertical component. The effect of azimuth, as indicated by the angles notated in the figure, is nominal. Hence, one structure for the vertical component suffices.

Several points are worth noting with reference to the figure. The vertical and horizontal components have very different effective ranges, viz., 25 ft and 250 ft, respectively. These numbers conjure a site with horizontal layers that are fairly uniform (large horizontal effective ranges), while variations of properties in the vertical direction are rapid (small vertical effective ranges). A small nugget value, 0.5 out of a total variance of 4.5, indicates that the background noise in the measurement is small.

With the help of the vmodel in Figure 7, the data from a finite number of measurement locations such as the RPSS can be extended to the complete site. This is done in two ways:

- By kriging, which amounts to interpolating and extrapolating the measurements to all points of the site using the vmodel, or
- By conditional stochastic simulation, which amounts to generating random realizations of the site according to the underlying vmodel and *conditioned* on the data points.

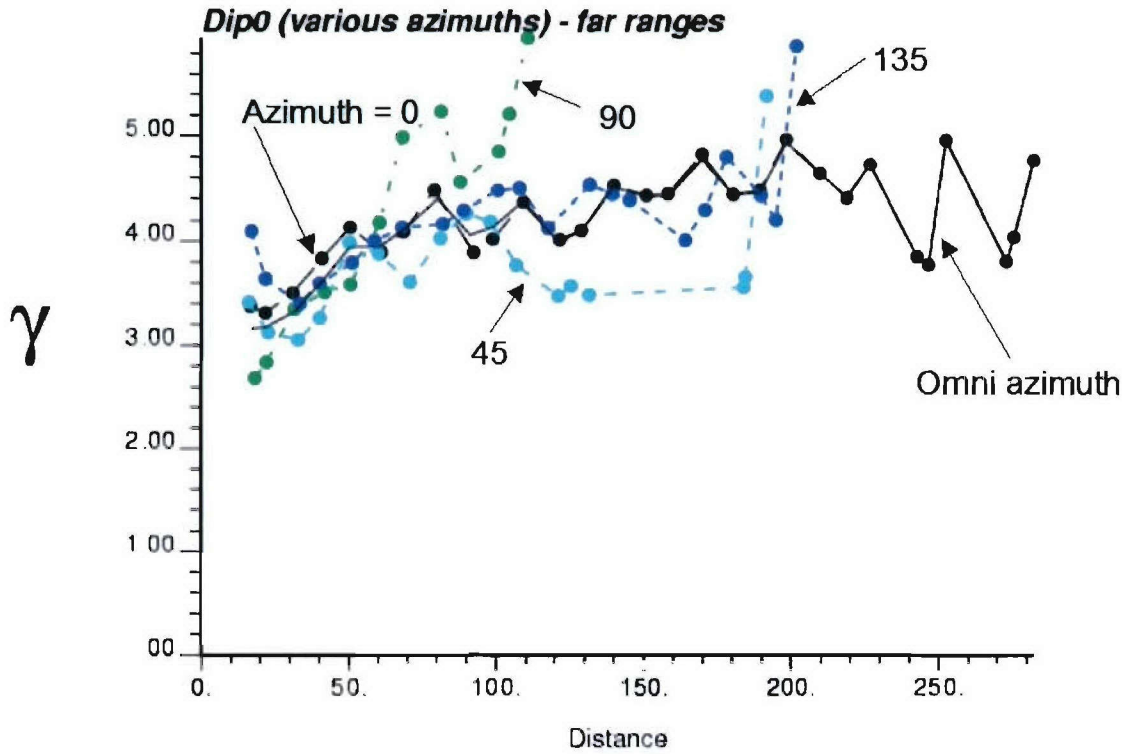

Figure 6. Variogram structure for RPSS index, λp; horizontal component. The effect of azimuth, as indicated by the angles in the figure, is also negligible. Hence, one structure for the horizontal component suffices. Details for separation distances less than 20 ft are not supported by data samples since no two RPSS sounding locations are closer than this distance.

Random fields generated by kriging and by simulation honor the measured data and the vmodel but have their respective unique characteristics (for details, see the many excellent texts available including Goovaerts, 1997[2]).

Continuing with the illustration based on the RPSS data of the demonstration site, the "kriging" results based on the data and the vmodel of Figure 7 are shown in Figure 8. The kriging estimates show a high λP layer around elevation 620 ft and a low λP layer at elevation 640 ft. If one equates the value of λP with rock quality, the profile given in the figure can be interpreted as a site with roughly horizontal layers, composed of a medium-rock matrix (yellow), with a weak layer embedded in the upper portion (cyan) and a strong layer embedded in the lower portion (red)[3].

[2] Goovaerts, P. Geostatistics for Natural Resources Evaluation, Oxford Univ. Press, NY, 1997.

[3] An independent study by Sandia, conducted and completed prior to our effort but also based on geostatistics, arrives at the same general conclusions about the site albeit with a slightly different variability structural model.

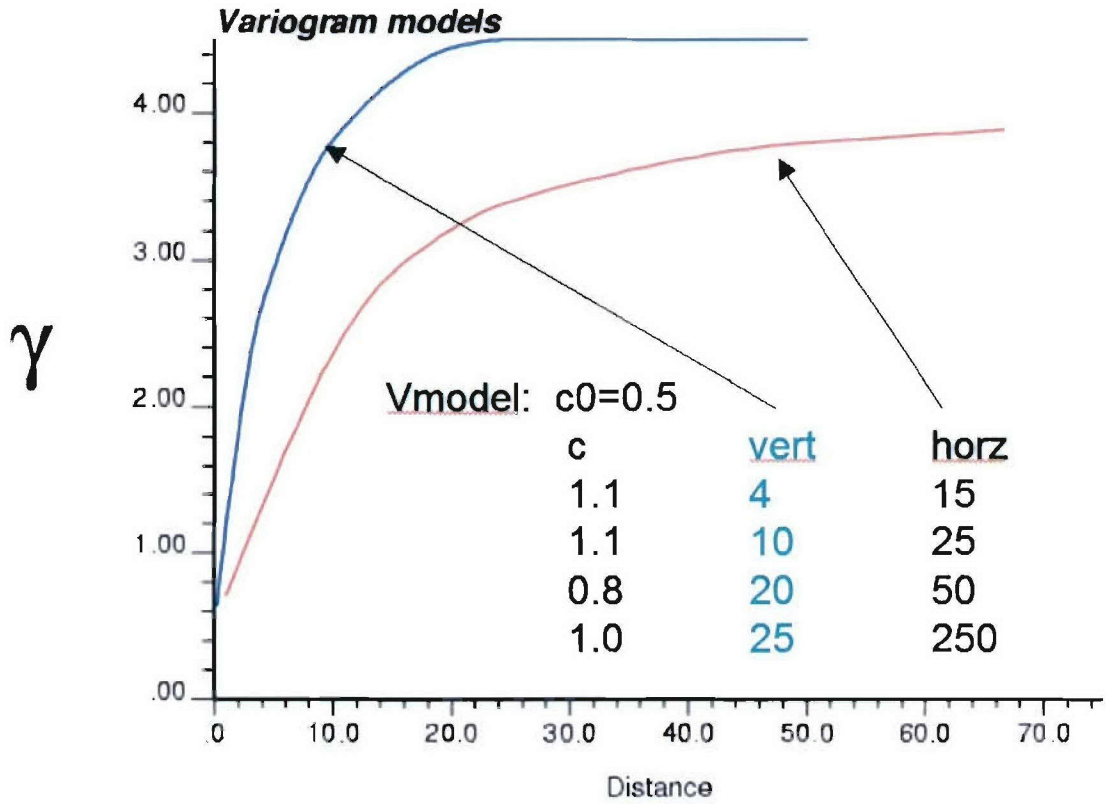

Figure 7. Variogram models based on the RPSS dataset, i.e., the curves are fitted to empirical data shown in Figures 5 and 6, respectively.

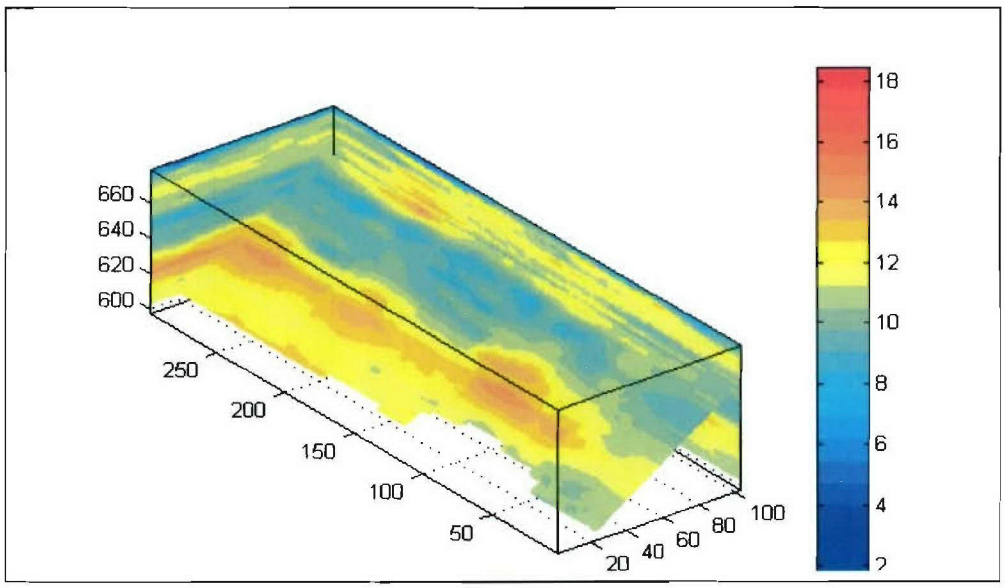

Figure 8. The technique of kriging extends λP from the 33 soundings to all points of the site. A cut-away view of the site volume of interest, measuring about 100 ft by 300 ft by 80 ft and divided into 3'x3'x2' cells (35 cells in x @ 3', 100 cells in y @ 3', and 40 cells in z @2'), is shown here.

Extension of the RPSS sounding data to the complete site was also carried out by means of (conditional sequential Gaussian) *stochastic simulation* technique, and the results given in Figure 9. The simulation results are more spotty (salt and pepper) than kriging results as expected - Kriging is an interpolation/extrapolation process and tends to smooth out the site profile; high values are under-estimated and low values are over-estimated, as is confirmed by the respective histograms given in Figure 10. On the other hand, because of their spottiness, simulation results are sometimes difficult to interpret although in the current example the strong (red) and weak (cyan) layers are clearly visible (Figure 10). But contrast them with the more prominent layers in the kriged field shown in Figure 9. Note also that while there is only one kriged field corresponding to the vmodel and a method of kriging (how interpolation and extrapolation are to be done), stochastic simulation gives rise to an infinite number of realizations, all conforming to the vmodel and the conditioning data points.

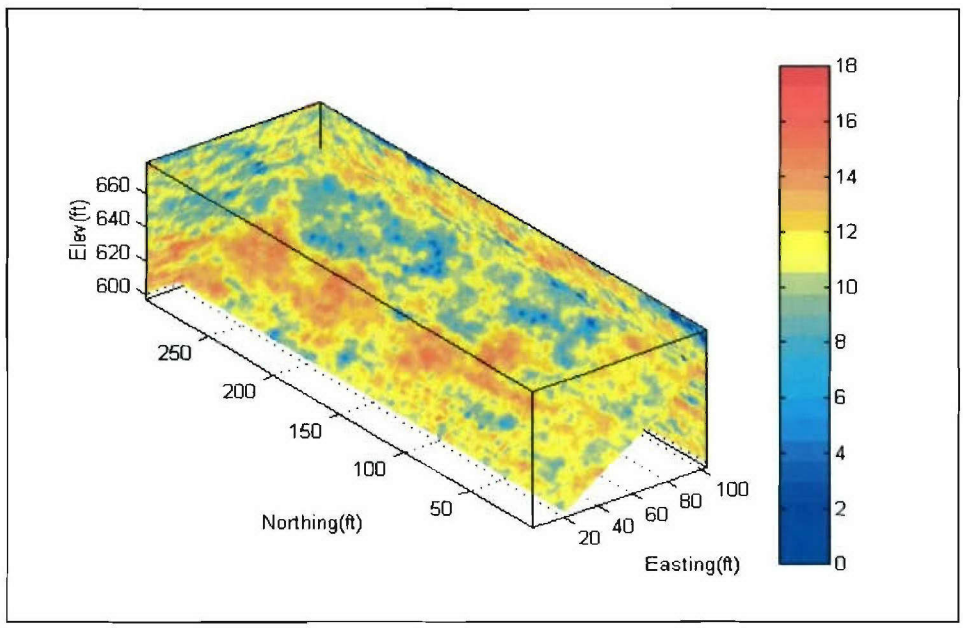

Figure 9. Extending the RPSS sounding data to the volume of interest by means of (conditional sequential Gaussian) stochastic simulation. The figure shows one of many realizations generated.

It should be obvious that the generalization of measured data to the complete field via the vmodel (either by kriging or simulation) depends on details of the variogram. In particular, decreasing the nugget reduces the spottiness and smoothes out the field, i.e., less noise; increasing the range does likewise. Sensitivity of the random field to these key parameters of the variogram has been investigated but details will not be shown here. As the database grows, e.g., more RPSS soundings, these key parameters become better defined and the uncertainty in the vmodel and, hence, the random field, decreases. Hence, the vmodel captures the data and their associated uncertainties; coarseness of data is reflected in a coarse vmodel.

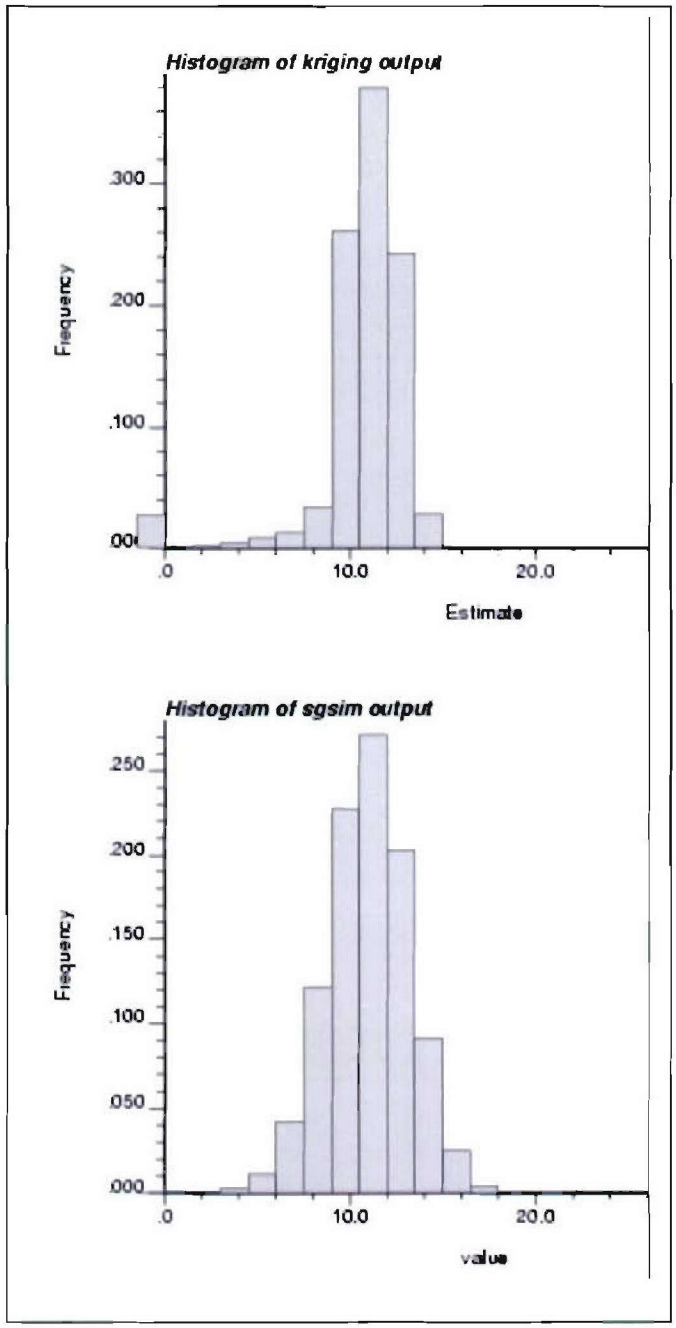

Figure 10. Comparison of histograms of the kriged and simulated fields. Kriged fields are smoother (less fluctuations; smaller variance)

Generate Fields of Rock-Mass Properties

As is well known, ground shock studies require characterizing the appropriate *rock-mass* property fields for the site. These properties include, among others, porosity, rock-mass rating, rock-mass bulk modulus and constrained modulus to the stress level of interest, rock-mass unconfined compressive strength, strength as a function of pressure, and void

closure strain. In addition, properties of the intact rock such as grain density, unconfined compressive strength and elastic moduli are needed to round out the material prescription.

We have demonstrated how random fields of certain *insitu* measurements, viz., the λP index from the RPSS soundings, can be generated by uncovering the underlying vmodel and using the vmodel to extend the data to the full site via stochastic simulation. Ideally, if the relevant intact and rock-mass properties required for ground shock studies are also measured to the same extent as λP, the stochastic realization process used on λP can be repeated to the measured rock-mass properties and the required random fields generated. But unfortunately, direct measurements of rock-mass properties are scarce. A larger body of intact properties exists, but it is also limited to what can be derived from samples taken from the (small number of) boreholes, and not from the (more numerous) RPSS soundings. The current state-of-technology is that rock-mass properties are inferred, based mainly on rock-engineering practices: they are inferred from the intact properties such as porosity (φ) then degraded based on estimates of rock quality such as rock-mass rating (RMR)..

That being the case, our demonstration followed the same strategy to derive rock-mass properties. But it is easy to see that other practices and schemes can be readily accommodated by the method and that feasibility of the overall approach being demonstrated does not depend on the particulars of how rock-mass properties are inferred. The important point to note is that as with any inference procedure, inference introduces an associated uncertainty which contributes to the overall uncertainty of the end product, i.e., the predicted ground shock environment. This uncertainty must be quantified and incorporated into the end product. We chose to side-step this uncertainty for the time being, so that we may focus on the generation of the random fields that enable ground shock simulation.

Accordingly, our procedure consists of two steps. First, (random) RMR and φ fields are generated from the laboratory and field data in the MQ database, mainly the *Vp* and *Vs* (compression and shear wave speed) data. Since these data exist in various degrees of completeness, and are largely limited to samples taken from the boreholes, their random fields are augmented by leveraging the vmodel of the more extensive measurements, viz., the RPSS sounding index λp introduced earlier. Second, the desired rock-mass property fields are generated by mapping from RMR and φ according to existing, well-accepted relations in rock engineering (e.g., Hoek et al, 2002).

Figure 11 gives an illustration of one of the random *insitu-Vp* fields obtained in the study. Note that variability exhibited in the data, as defined by the borehole samples (sub-figure b), is retained in the generated random field (sub-figure c). The insitu-*Vp* field is mapped to the porosity field using the empirical data summarized in Figure 12, ending with the result shown in Figure 13.

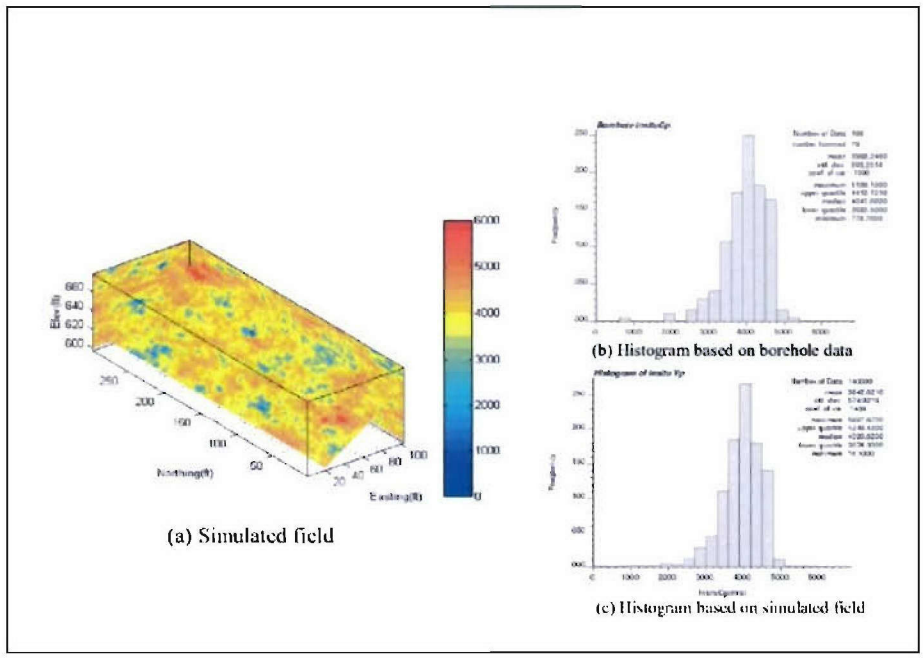

Figure 11. Simulated insitu-*Vp* field. The figure shows one of many random samples generated.

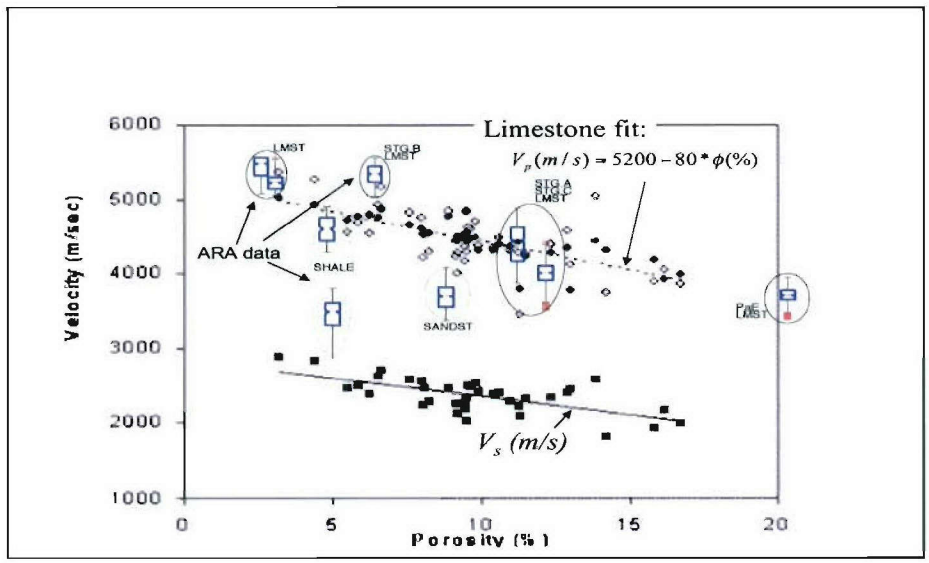

Figure 12. Mapping between insitu-*Vp* and porosity for limestones. Whisker data are from the MQ database. Backdrop data are taken from: Assefa, S., McCann, C., and J. Sothcott, Velocities of Compressional Waves and Shear Waves in Limestones, Geophysical Prospecting, 2002.

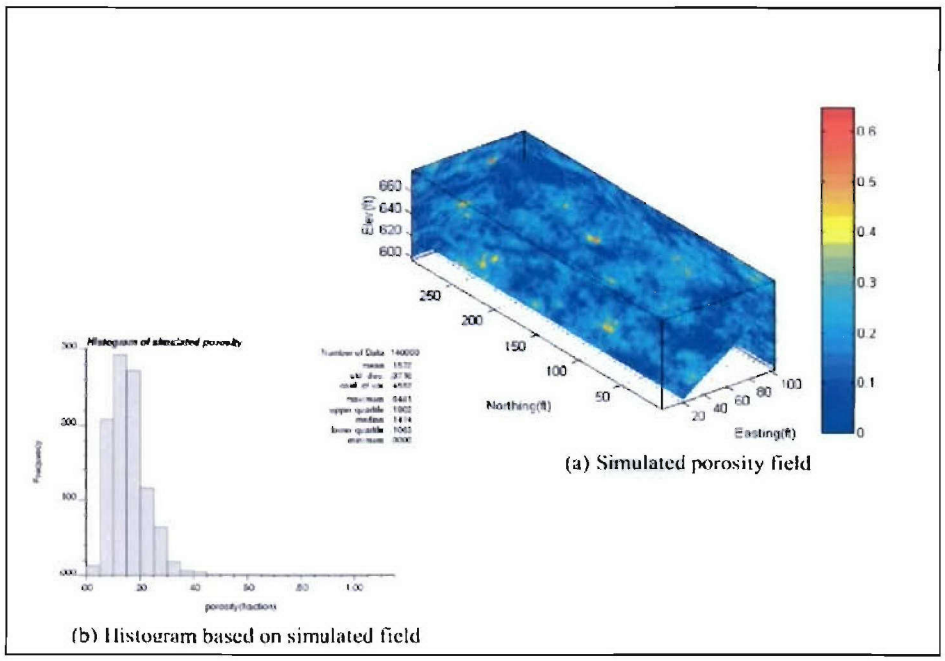

Figure 13. Porosity field corresponding to Figure 12.

Similarly, random RMR fields based on the square of the velocity ratio, i.e., $(insitu\text{-}Vp/\text{intact-}Vp)^2$, are generated, and a sample field is presented as Figure 14. Direct information on RMR can also be found in the MQ database, and can be incorporated in the simulation process as conditions. We have not done so because of uncertainty in interpreting the data and limited resources available.

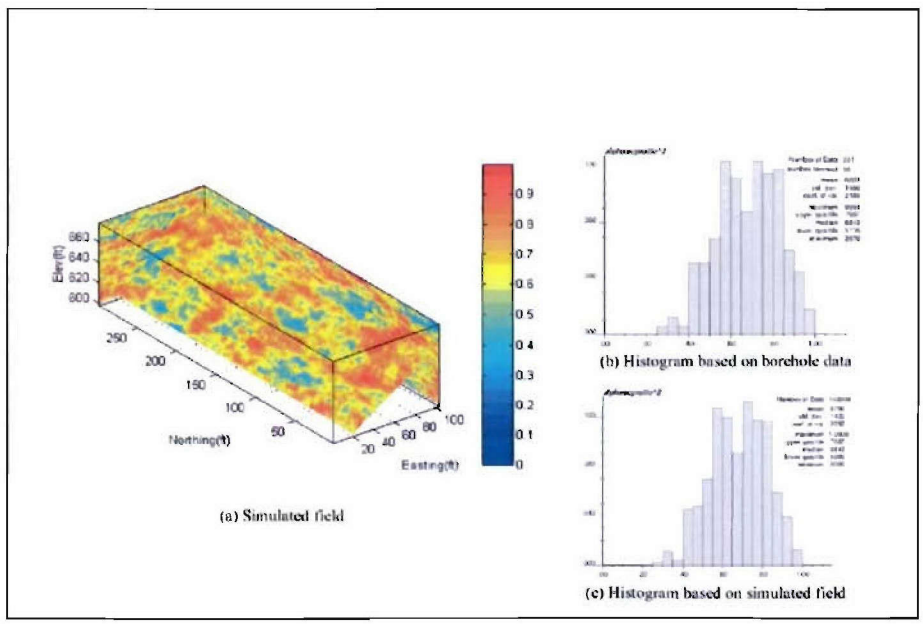

Figure E-14. Simulated RMR field based on square of the velocity ratio.

In the second step, given a particular rock type, e.g., limestone (for this exercise, we assumed that the sandstone & shale layers at MQ were limestone), and a porosity φ, generic relations enabled us to look up the corresponding intact properties. Using the RMR information, we were able to map the intact properties to *insitu*-properties and, finally, to rock-mass properties using rock-engineering guidelines. Details will be skipped, but two properties are singled out for illustration below: The constrained modulus M, and the unconfined compressive strength UCS.

The intact constrained modulus undergoes a two-step reduction, to become the rock-mass constrained modulus:

$$RMR * M^{lab} \Rightarrow M^{insitu}$$

$$\beta * M^{insitu} \Rightarrow M^{rockmass}$$

where

$$\beta = \begin{cases} 0.15 & \text{if } RMR \le 60 \\ -1.125 + 0.02125 * RMR & \text{if } RMR > 60 \end{cases}$$

is a modulus reduction factor attributed to experimental data obtained by Stagg & Zienkiewicz (1974). And the rock-mass strength is related to the intact strength by:

$$r_s * UCS^{lab} \Rightarrow UCS^{rockmass}$$

$$r_s = \sqrt{e^{(RMR-100)/9}} \quad \text{undisturbed}$$

This relation is attributed to Hoek & Brown (1980, see www.rocscience.com).

$$r_s = \sqrt{e^{(RMR-100)/6}} \quad \text{disturbed}$$

Sample results are given in Figure 15:

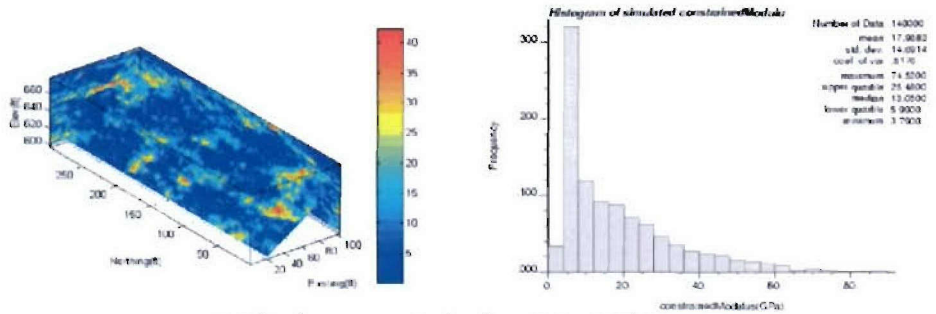

(a) Rockmass constrained modulus (MPa)

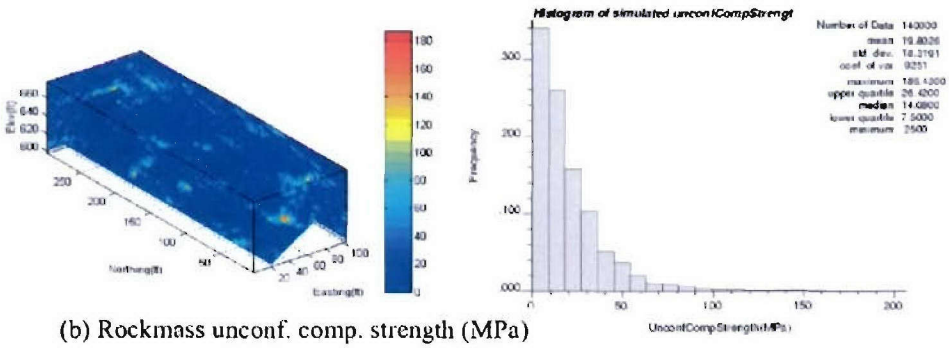

(b) Rockmass unconf. comp. strength (MPa)

Figure 15. Sample realizations of the rock-mass constrained modulus and rock-mass unconfined compressive strength.

Perform Stochastic Finite-Element Simulation of Ground Shock Propagation

Stochastic finite-element simulation refers to the repeated application of a *deterministic* finite-element ground-shock simulation tool to realizations of the random field. Each application takes one realized random field, performs a deterministic ground-shock simulation, and generates a deterministic ground-shock response. When all is said and done, each realization of the random field will have a ground-shock field counterpart. The variation in the ground-shock response from realization to realization defines its uncertainty, which can be attributed solely to the uncertainty in media properties since the energy source is also deterministic – it is the same for all simulations. This was done so we could focus on the effects of media properties.

Deterministic finite-element simulation of ground-shock propagation is quite straightforward given the prevalent use of finite-element tools in the community. The following may be note-worthy:

Assignment of rock-mass properties to the elements – The volume of interest is discretized into three-dimensional brick elements, each of which is assigned rock-mass properties that correspond to a realization of the random field described previously. The rock-mass properties are uniform within an element, but the rock-mass properties of a given element will, in general, vary from realization to realization as dictated by the

stochasticity of the random field. The element size is an important issue, especially in relation to the cell size used in generating the random fields; the element size may be different from the cell size. For simplicity, we chose an element size that is the same as the cell size, viz., 3'x3'x2'.

Implementation of properties in a constitutive model - The next step in the simulation is to implement the rock-mass properties of an element in a constitutive model, so that it can be exercised by the ground-shock code. The choice of constitutive model (and its computer implementation) is usually constrained by the ground shock code used; each finite-element tool has its own material modeling preference. Our use of FLEX[4] in this demonstration, for example, required that the rock-mass properties be implemented in a SFT1 model[5]. Suffice to say that the same set of rock-mass properties may be implemented in different constitutive models for use in various ground-shock codes, and the various implementations/codes will not in general produce the same result.

For our purpose, a set of SFT1 parameters was generated to correspond to a particular set of prescribed rock-mass properties. The SFT1 parameters are then incorporated as one "material type" in the material library, so that they can be exercised in a simulation. The determination of the SFT1 parameters from prescribed rock-mass properties is not trivial; it is a source of uncertainty in its own right. Furthermore, since rock-mass properties have continuous valuation within their respective ranges of variation, we have, in effect, an infinite number of material types in the library. This, obviously, cannot be, and we circumvented the difficulty as described in the following.

(a) In order to keep the number of materials reasonable, we picked 10 discrete values of RMR ($0.5<RMR<1.0$), and 10 discrete values of porosity ($0< \varphi <0.2$). This resulted in 100 unique (RMR,φ) pairs and hence 100 unique materials. For each cell in each realization, we simply assigned the material with the closest (RMR, φ).

(b) To construct nonlinear SFT1 models from the (RMR, φ) values we adopted the rock engineering correlations recently published by Chitty[6]. Chitty's report became available during the course of this investigation. It includes many of the accepted rock engineering relations mentioned above, and extends them into the higher pressure regime relevant for shock propagation. Chitty's work infers most of the Limestone strength and compressibility information needed to construct models such as SFT1 based solely on porosity and RMR. These relations are generic for limestone, but we note that MQ data are included in the data base used to generate the generic relations. We wrote an automated procedure to

[4] Vaughan, 'Flex User's Manual, Version 1-J9.1,', Weidlinger Associates, 2005.
[5] Mould, J. C. and H.S. Levine, " A Rate-Dependent Three Invariant Softening Model for Concrete," Mechanics of Materials and Structures, Voyiadjis, G. et. al. ,eds, Elsevier, Amsterdam, 1994.

[6] Chitty, D.E., "A Unified Methodology for Estimation of Rock mass Properties and Associated Uncertainties to Support Characterization of Inaccessible Sites," DTRA Test Operations Technology and Test support, June 2005.

generate SFT1 model parameters based on the Chitty correlations, augmented by some further assumptions on rate effects, extension to compression ratios, etc.

Finite-element modeling and ground-shock parameters

The finite element analyses for ground-shock simulations were performed using the 8-noded hexahedron element of the FLEX code. The box shaped study area was discretized into 3'x 3'x 2' finite elements. For the region near the explosion source, however, a finer finite element mesh was used to resolve the explosive charge. The explosive source and adjacent region were modeled using the FUSE capability[7] of the FLEX code. The source was a 51.875 inch diameter sphere of Nitromethane – the same as in the DG-1 and DG-2 experiments. This was modeled using the JWL equation of state for Nitromethane. In general, this approach has proved satisfactory for ground shock calculations. For this exercise, the source was placed in the center of the characterized region of the test bed rather than at its perimeter. The top face of the model was free, while the other five faces were restrained using absorbing boundary conditions. Each analysis was performed for a period of 10 milliseconds and the peak hydrostatic pressure, peak compressive principal stress and peak velocity magnitude during this period were recorded for each element. These aspects of the calculation remained unchanged for all realizations of the site

Ground-shock realizations - We have performed two series of stochastic finite-element simulations using the WAI FLEX code and the SFT1 constitutive model, and the results are summarized herein. As a first try, we generated 20 realizations of the site based on the vmodel as described in a previous section. Each realization was then used in a ground-shock simulation calculation subjected to the same energy source. Important free-field measures, such as peak pressure, peak principal stress, peak velocity, etc. were monitored throughout the site. Hence, we obtained 20 ground-shock realizations (free-field environments) that corresponded to the site realizations. We denote the results from this series as "WAI site", for lack of a better term.

In the second series, we repeated the exercise for a slightly different stochastic site model (derived based on a slightly different interpretation of the same database; see Sandia report). Again, the same finite-element set up and energy source was used so that the only variable was the site property realization. These results are referred to as the "S2 site".

We have also performed a reference calculation: The free-field environment was predicted based on a deterministic site model which corresponds to the uniform, layered site geometry used by the community in the DG2 exercise. We call this reference the "layered site"

To give a flavor of what a stochastic ground-shock environment is like, we compare in Figure 16 one realization for the WAI site (sub-figure (a)) with one for the S2 site (sub-

[7] Sandler, I.S., "A new Computational procedure for wave propagation problems and a new procedure for non-reflecting boundaries," Computer Methods in applied mechanics and engineering, Vol. 164, 1998.

figure (b)). Sub-figure (c) shows the environment from the (deterministic) layered site, introduced for reference. The attribute plotted is the peak pressure, in MPa. For clarity, the figure features a center-cut of the volume (viz., an Easting slice) and two background cuts for 3D effects.

The peak pressure is highest at the source, as expected, which is indicated by the red square[8] at the center of each sub-figure. But since the source pressure is high (~ 3,500 Mpa), it dominates the rest of the field so that in this, the default magnitude scale, differences among the sub-figures cannot be discerned readily.

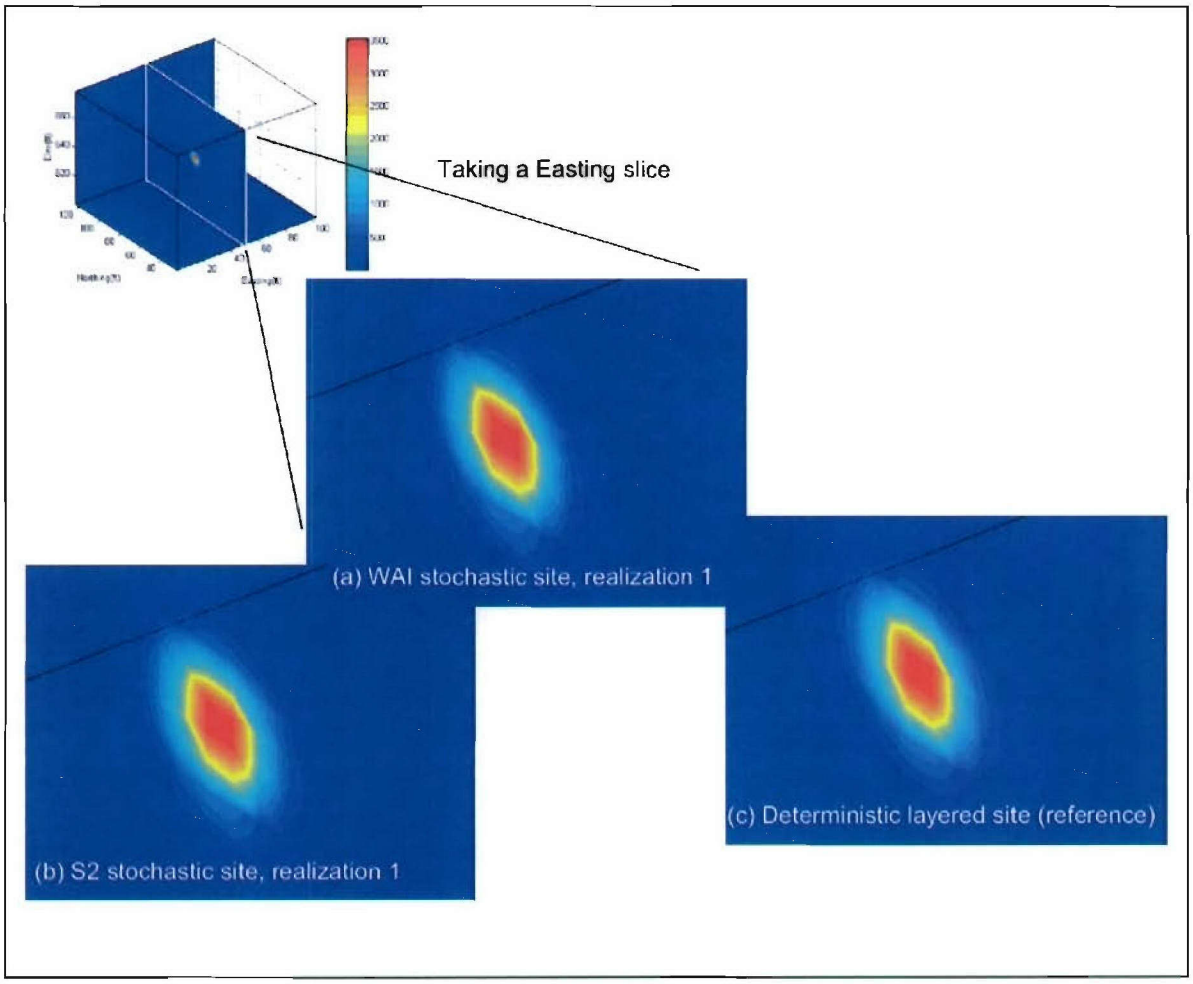

Figure 16. Comparing a ground-shock realization for the WAI site and the S2 site; the result from the deterministic layered site serves as reference purpose only.

[8] Note that while the source is modeled as a cube (by the FUSE module), the ground-shock environment further away from the source is roughly spherically symmetrical as one would expect, despite the presence of layers.

To see the lower-pressure regions more clearly, we limit the magnitude to 100 MPa, and the comparison is re-plotted as Figure 17. The layered site in sub-figure (c) exhibits a fairly spherically symmetric environment, which is only tempered by the presence of layers. On the other hand, the environments at the stochastic sites are much less symmetrical. There is a strong angular dependence in the featured cut – shades of a shooting star, versus a fireball. The "weakly connected" layered features in the background cuts become more prominent, reminiscent of the layered features in the stochastic site-property fields.

To see yet more details of the lower-pressure regions, the cut-off is lowered to 25 MPa and the results presented in Figure 18. The fireball becomes more ragged, and the layers "connect", become stronger in presence, and show more discontinuity especially when compared with the reference. The WAI site and S2 site results are fairly similar in general features, albeit they can be very different when compared location by location – hence, stochasticity. At a particular location, the variation from realization to realization can be large and difficult to grasp, exactly the experience we had with site properties.

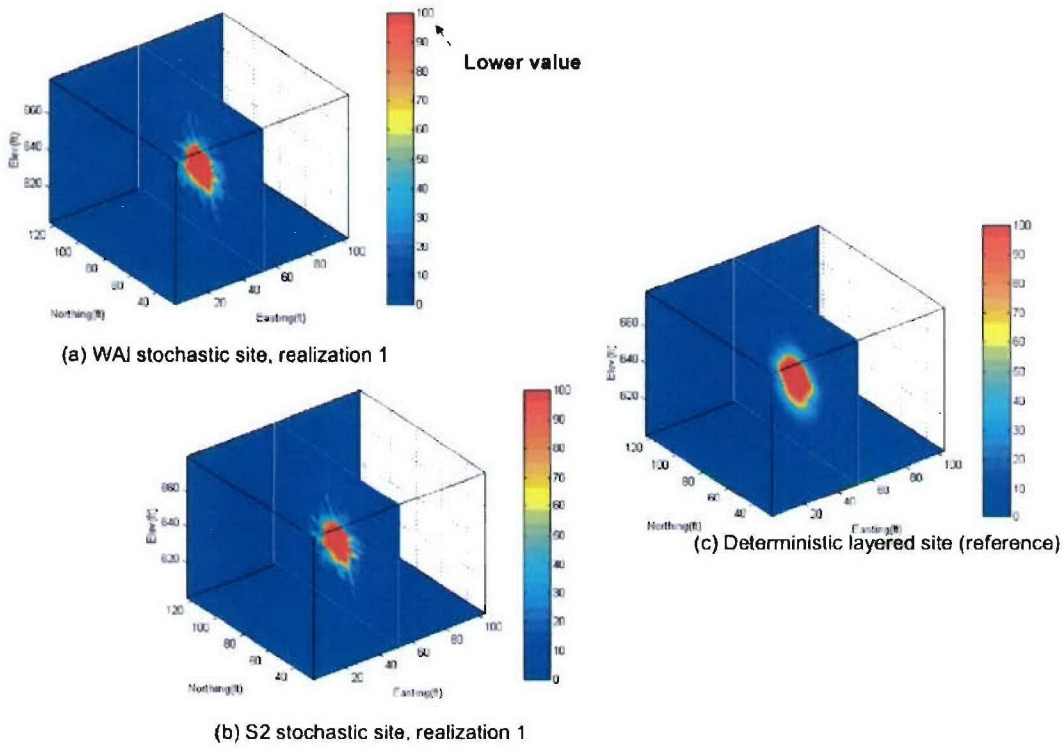

Figure 17. Same as Figure 16, but with the magnitude scale limited to 100 MPa.

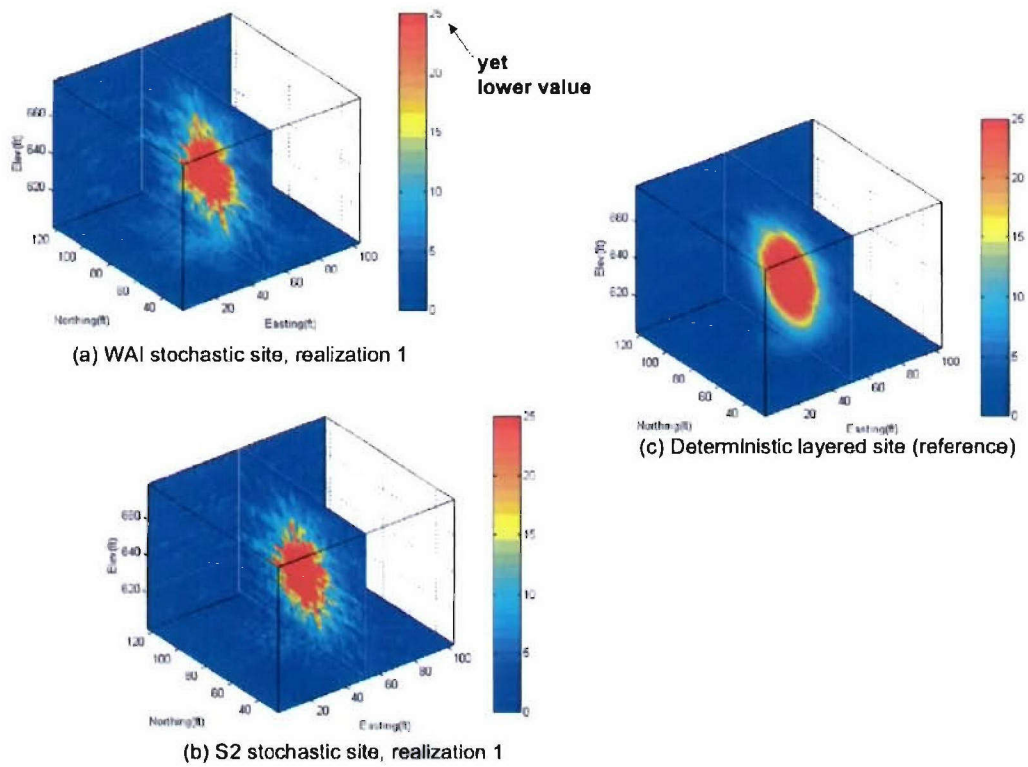

Figure 18. Same as Figures 16 or 17, but with the magnitude scaled limited to 25 MPa.

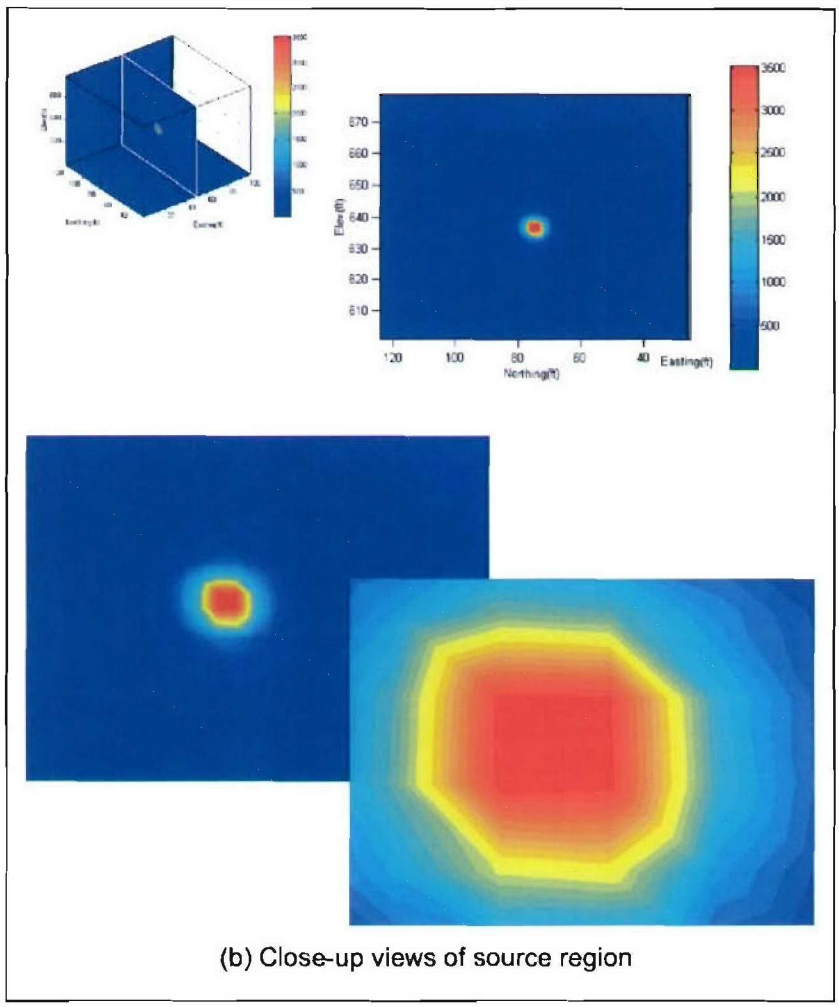

(b) Close-up views of source region

Figure 19. Sample mean based on realizations for the WAI site. Attribute plotted is peak pressure, in MPa.

Quantify Local and Spatial Variability of Ground-Shock Response

The purpose in generating the sets of alternative realizations is so we can extract information from them to quantify the uncertainty in the ground-shock environment. Qualitatively, one can get a feel of the uncertainty by showing the realizations visually one at a time but in rapid succession, like frames of an animated cartoon[9]. Quantitatively,

[9] Like an animated cartoon, successive realizations must be similar enough to allow the eye to catch gradual changes. The animated display of realizations allows one to distinguish areas that remain stable over all realizations (low uncertainty) from those with large fluctuations between realizations (high uncertainty).

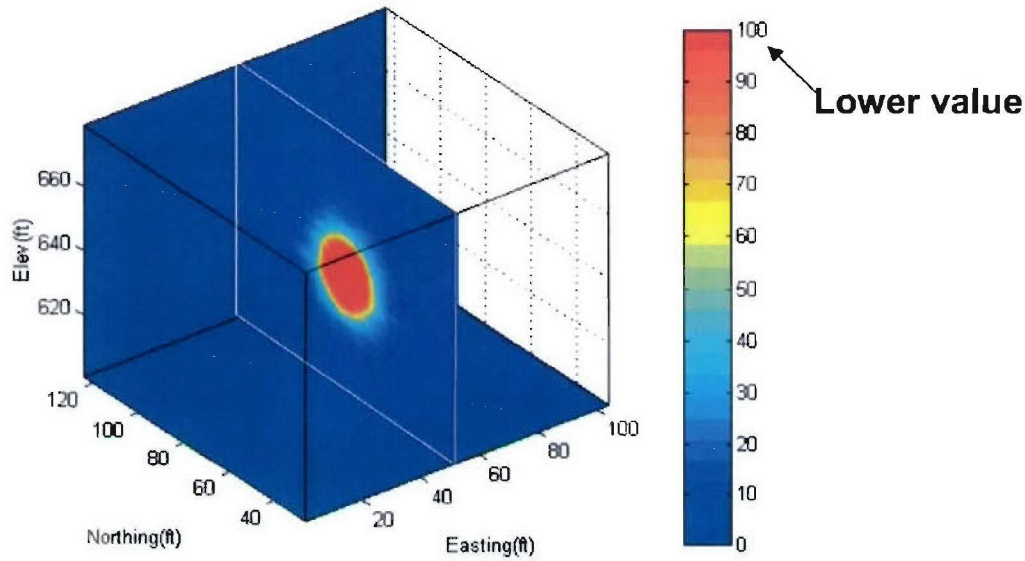

(a) Same as previous chart, but focusing on lower magnitudes

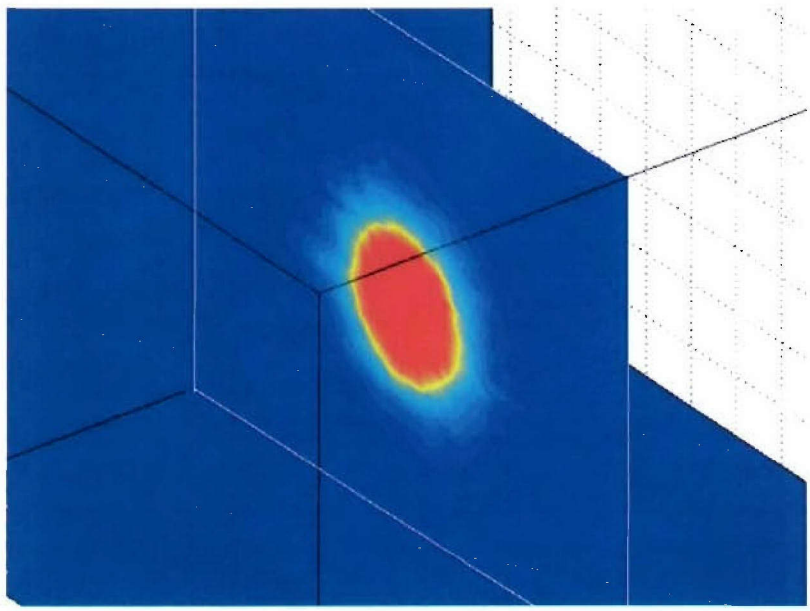

Figure 20. Same as Figure 19 but with the magnitude scale limited to 100 MPa to show details of the lower-pressure regions.

there are two aspects to the uncertainty: Local (point) and spatial (global). We discuss them further in the following.

Local uncertainty is quantified by the sample mean and variance, which are typically combined to derive a (Gaussian-type) confidence interval centered on the mean value[10]. With more assumptions, the sample mean and variance can be parlayed into a local probability distribution.

Figure 19 gives the sample mean of the ground-shock realizations for the WAI site. Again, because of the dominance of the source region on peak value, one only sees the source in this magnitude scale and not much else. We circumvent this difficulty as before by limiting the scale to 100 MPa, and the results are shown in Figure 20. In the lower pressure region, the sample average is fireball like – much like its deterministic (layered-site) counterpart given previously in Figure 17(c).

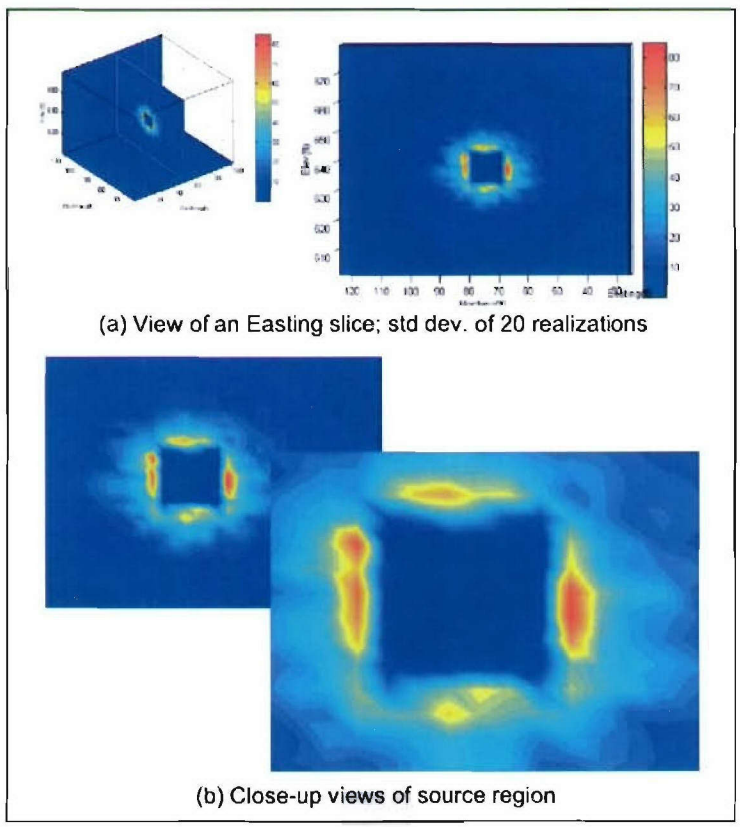

(a) View of an Easting slice; std dev. of 20 realizations

(b) Close-up views of source region

Figure 21. Sample standard deviation, WAI site, default magnitude scale. Source region has zero deviation since it is deterministic – same source is used for all realizations.

[10] For example, the 95% confidence interval is taken as

$$\Pr\{Z(u) \in [z^*(u) - 2\sigma(u), z^*(u) + 2\sigma(u)]\} = 0.95$$

where $z^*(u)$ is the sample mean and $\sigma^2(u)$ is the sample variance at location u computed from the stochastic realizations

Likewise, we show the sample standard deviation in Figures 21 and 22 in two magnitude scales. The plot in default scale, Figure 21, is dominated by the near-source region – which has the largest standard deviation. Note that the source itself has zero standard deviation since it is deterministic! In the lower magnitude scale, Figure 22, the heterogeneity shows up very strongly.

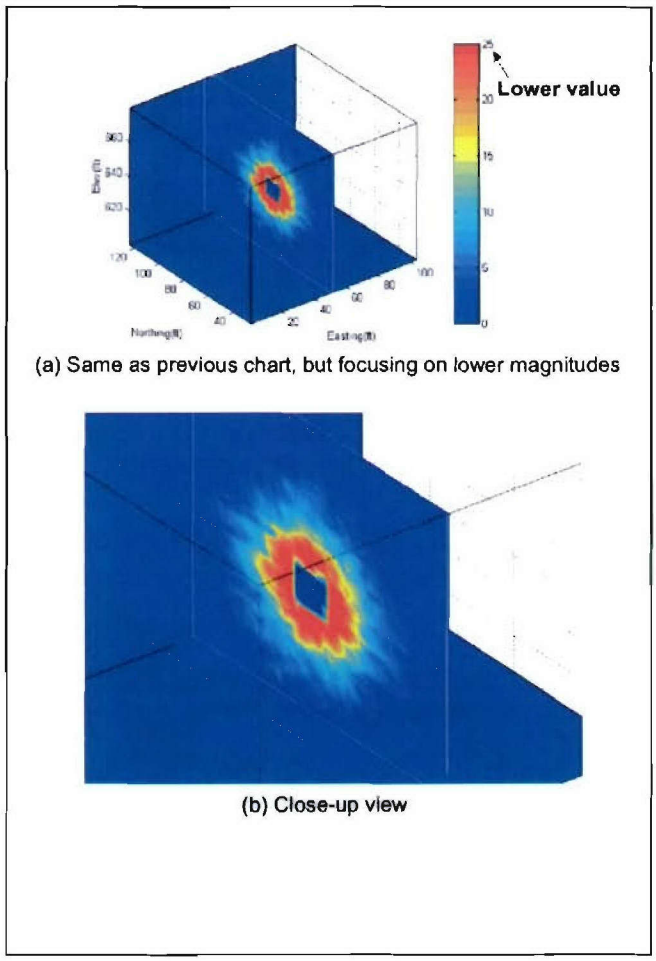

Figure 22. Same as Figure 21, but limited to values 25 MPa and less.

The WAI site results are further compared with the S2 site results in Figure 23, to give an idea of the sensitivity to slight variations in the site vmodel. A couple of points are noted:

(1) Higher pressure regions (other than the source region itself, which is deterministic) have higher standard deviation
(2) Spatial distributions of the two stochastic sets are similar; differences are reminiscent of those observed in a comparison of the site realizations – S2 has a stronger layered structure.

Hence, it is desirable to use a measure for variability that is independent of the ground-shock magnitude. This prompts us to look to the coefficient of variation, which is the sample standard deviation normalized by the sample mean and commonly denoted as COV. As can be seen from the comparison in Figure 24, the COV runs between 0 and 1, with higher COVs distributed near the source and lower COVs further away from the source. The S2-site COVs exhibit a stronger layer structure; the WAI-site results are more salt-and-pepper. The histograms on the right side of the figure indicate that the two COV distributions are in fact very similar. Mean value of the WAI-site COV is slightly larger, indicating slightly greater variability in the WAI-site ground-shock environment. This is a direct result of the higher variability in the site model, as was mentioned in a previous section.

Finally, using the sample mean and standard deviation (or COV), bounding fields such as those based on mean ± n*standard deviation, where n is an integer, can be generated. For example, Figure 25 gives the (mean ± 1 standard deviation) bounds. The uncertainty in ground-shock at any location in the field, in this case the peak pressure, is thus delineated.

It is obvious that other ground-shock attributes can be processed in identical fashion. This is not done due to time and budget limitations.

Spatial uncertainty of ground-shock, like that of the site properties, requires a measure of the joint uncertainty about ground-shock values at several locations taken together – e.g., the probability of occurrence of a string of high peak stresses or low stresses. Such information can be extracted from the stochastic fields using the same geostatistics techniques used for site characterization. Alternately, the uncertainty information can be summarized using different types of metrics including: Probability maps, quantile maps, and maps of spread. These directions will be explored in a subsequent study.

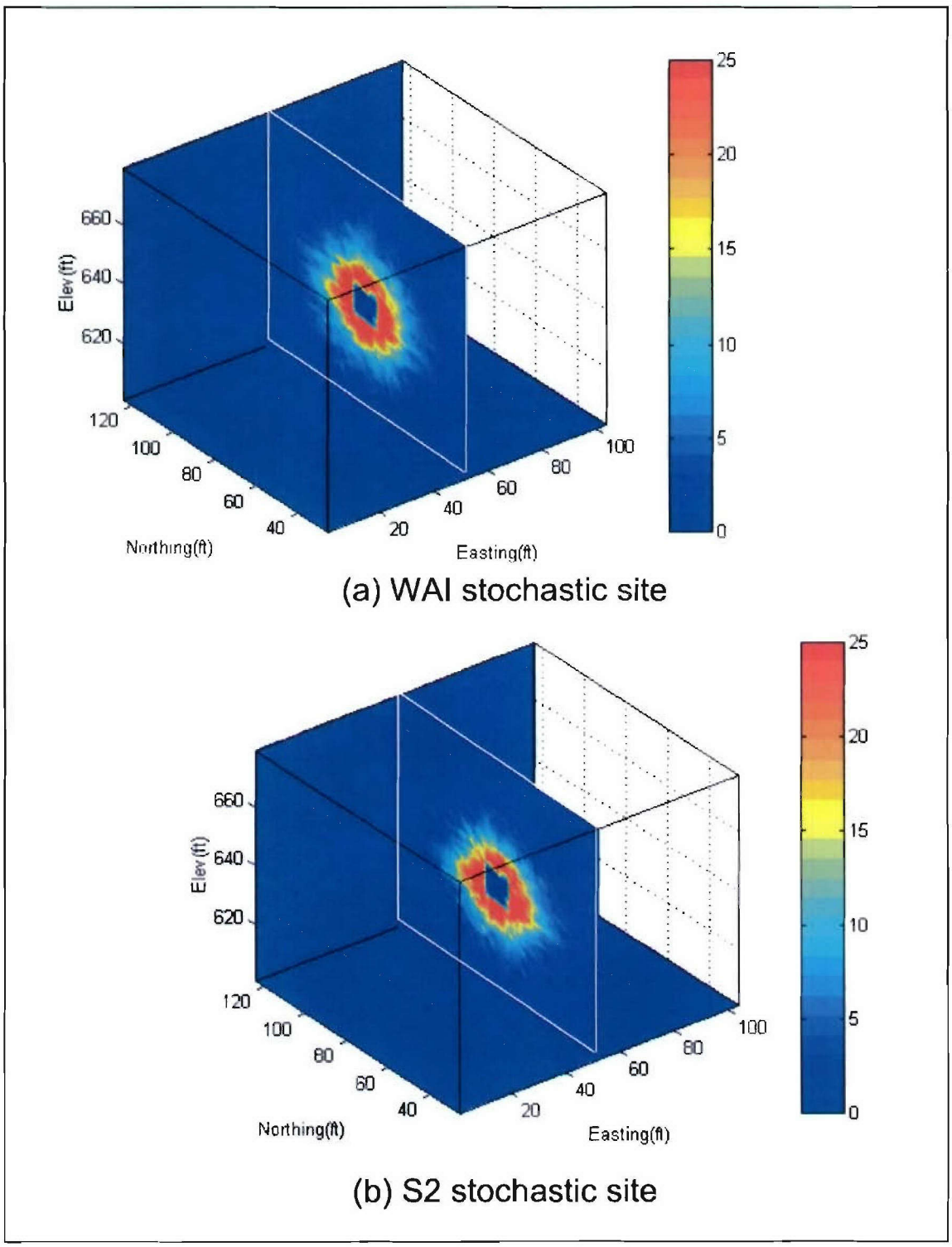

Figure 23. Comparison of sample standard deviations, realizations for WAI site and the S2 site.

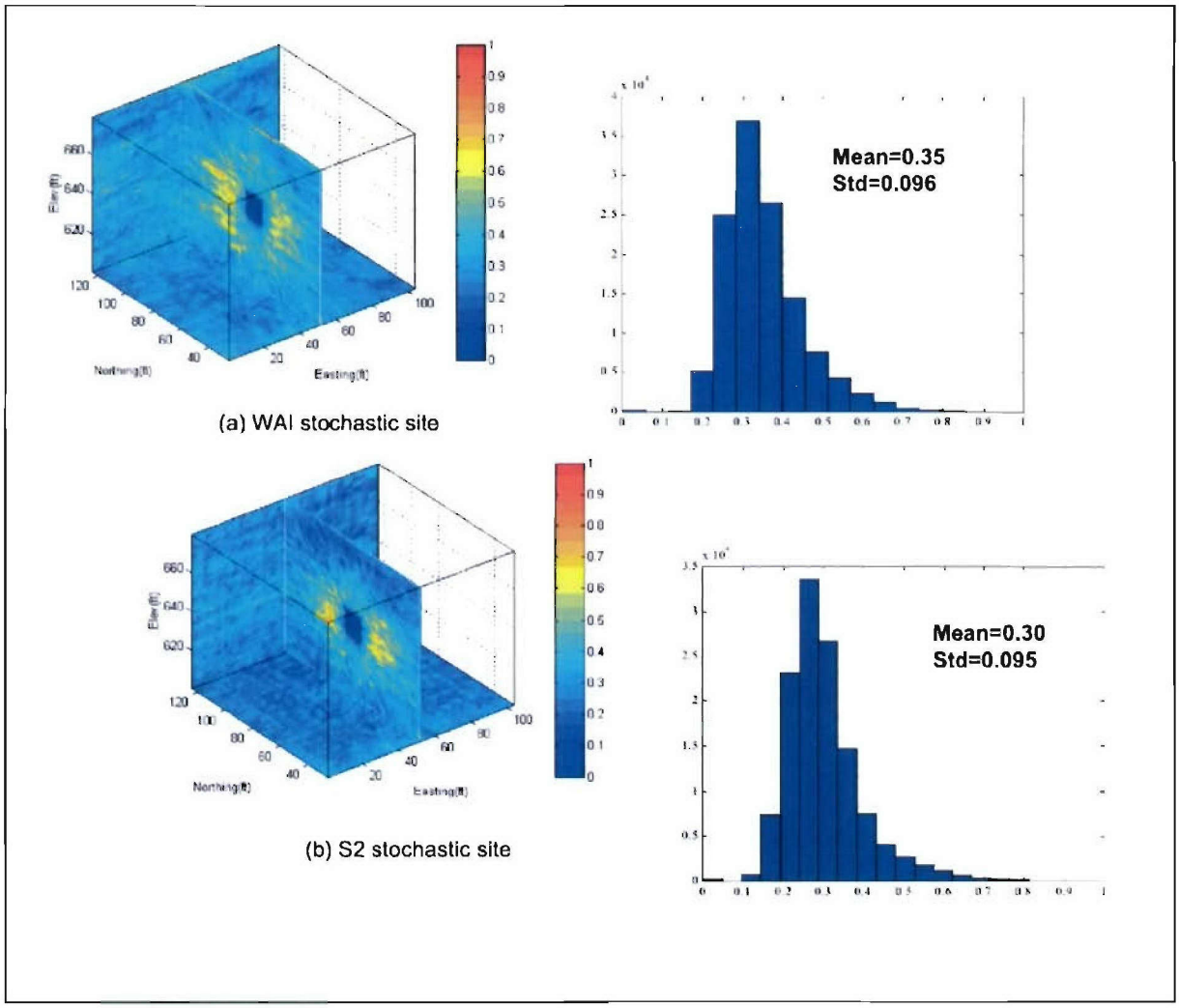

Figure 24. Comparison of COVs based on realizations for the WAI site and the S2 site.

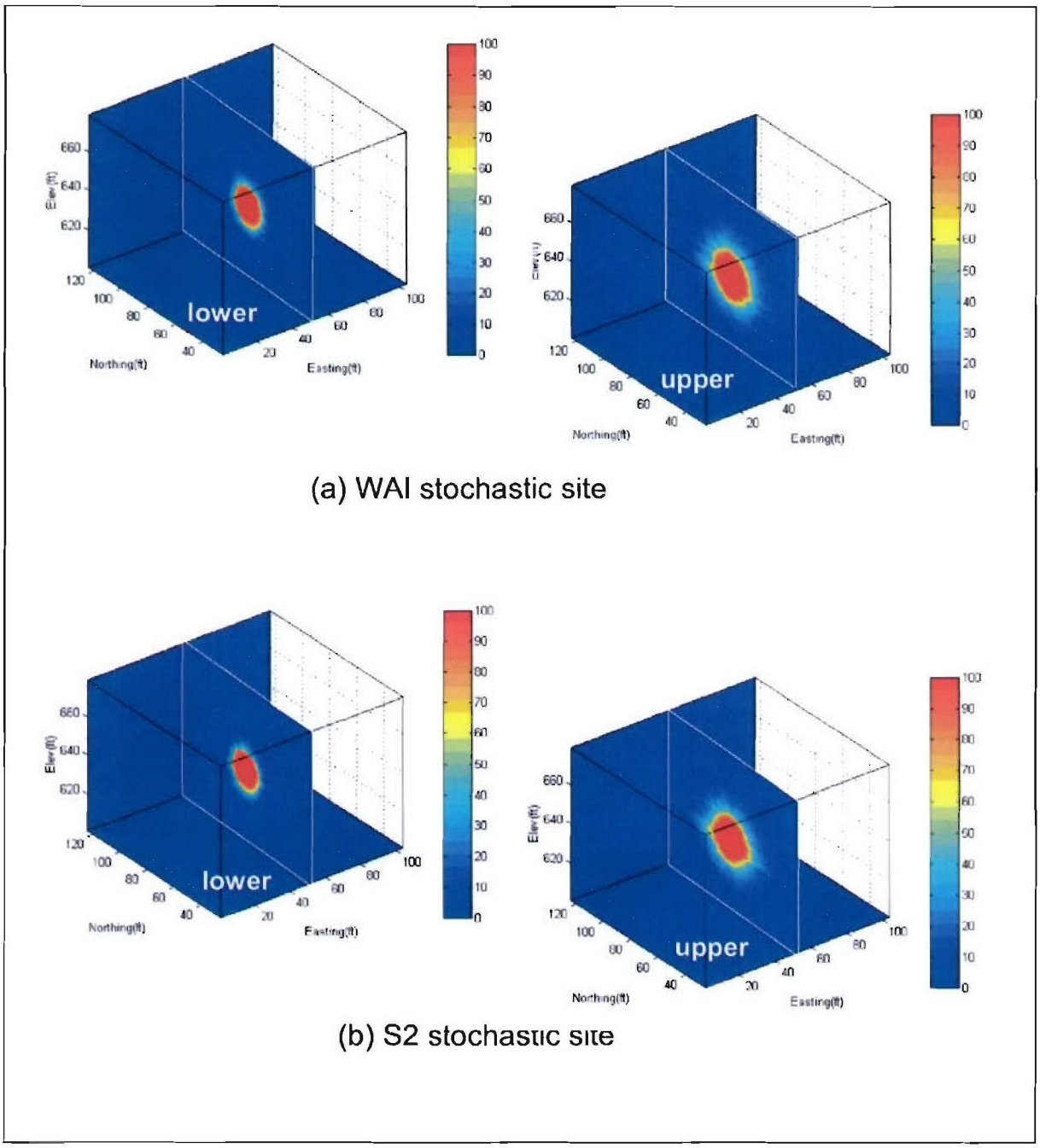

Figure 25. Upper and lower bounds of peak pressure, as measured by (sample mean ± 1 standard deviation).

As a final point, figures 26 and 27 compare velocity waveforms from several stochastic realizations to that from the conventional layered approximation. Note the smoother appearance and slightly different structure of the heterogeneous sites relative to the layered site. Though not analyzed in this report, we find these differences very interesting.

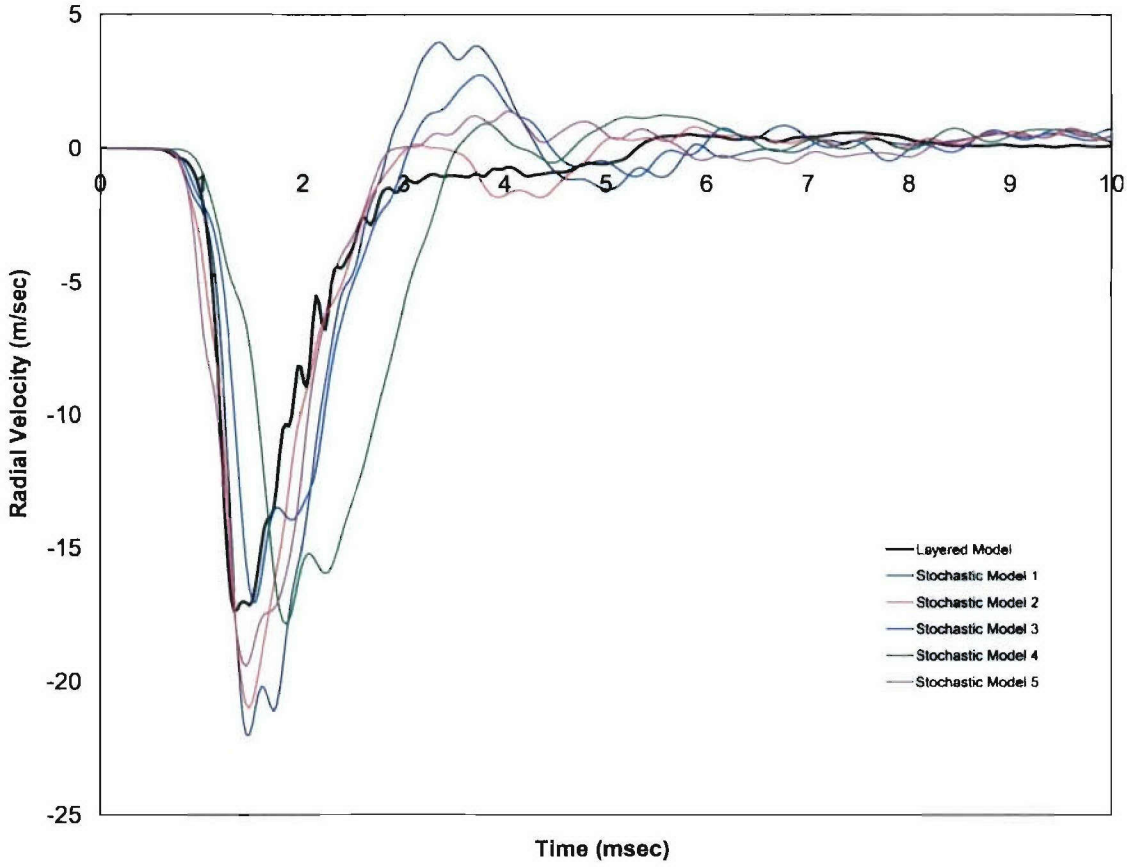

Figure 26. Radial velocities 13.5 ft. below charge.

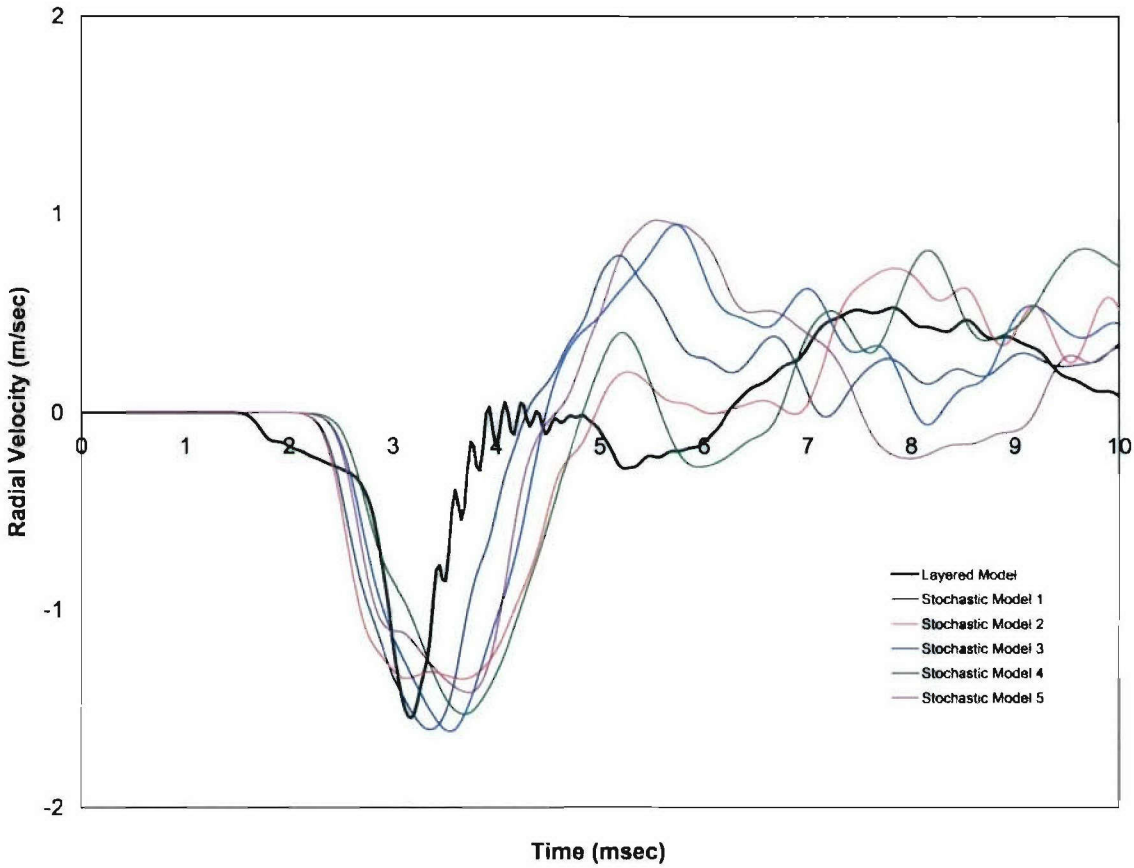

Figure 27. Radial velocities 34.6 ft. below charge.

ACKNOWLEDGMENT

The work described herein is sponsored by DTRA under a 2004 SBIR Phase I award. The technical monitor is Robert Reinke of DTRA/TDTTP, who called to our attention the Mitchell Quarry project that was instrumental to the study. It served as a handy demonstration test bed. Various agencies and organizations have provided us with useful data that facilitated our study, notably Dan Chitty et al at ARA and Sean McKenna et al at Sandia. We would like to thank all of them.

The project is an outgrowth of ideas contributed by Felix Wong, Victor Pereyra and John Mould of WAI, and Tapan Mukerji, Gary Mavko and Jack Dvorkian of PCI. These gentlemen also contributed to the writing and preparation of this report. We want to thank Reza Salari of WAI, the FLEX analyst most responsible for performing the finite-element simulations reported herein.

All geostatistics processing mentioned in the report was performed using GSLIB, the software package put out in the public domain by Clayton Deutsch and Andre Journel of Stanford University. Our study would have been difficult, and our progress slow if they had not made the software library available. We also found its companion, WinGSLIB from www.statios.com very helpful.

HYPERLINKED TEXTS

Appendix A. Selected Sandia Results

We compare the vmodel developed herein with those discussed in the Sandia report, for reference purposes. All variograms have been normalized to have a sill value of 1 for easy comparison. The model labeled WAI is the model developed from data from the 33 RPSS soundings as described in the main text. The model labeled Sandia1 (S1) corresponds to that given in the Sandia report based on 23 RPSS soundings (Phase 1 site exploration, Table 3 of Sandia report), whereas the Sandia2 (S2) model corresponds to that given in Table 6 of said report for a subset of the volume of interest.

With reference to Figure A-1, the vertical variograms for WAI and S1 are identical, for all practical purposes. The horizontal variograms differ in two important aspects: the range and asymptote. In particular, the effective horizontal range is about 100+ ft for WAI and only 15 for S1. Hence, one expects the S1 field to be choppier horizontally.

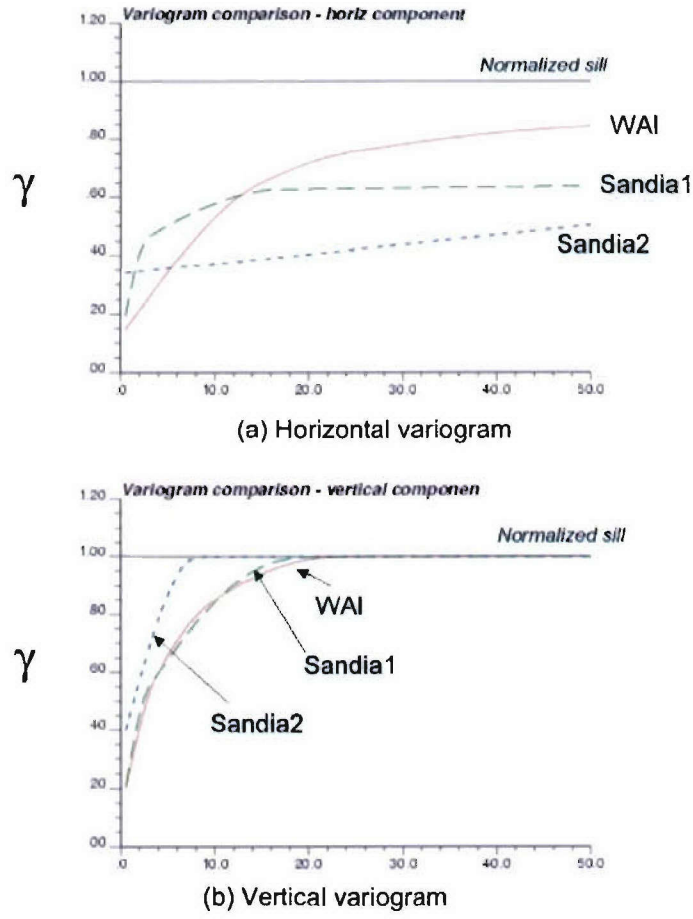

Figure A-1. Comparison of vmodels generated herein and in said reference.

Compared with the WAI model, the S2 model has a smaller vertical range (8 ft versus 20 ft), and a *larger* horizontal range (over 200 ft, versus 100+ ft). Hence, one expects the S2 field to be more choppy vertically, but very uniform horizontally. These effects are confirmed by the corresponding simulated fields given in Figure A-2. Note the correspondence between large effective horizontal ranges (Sandia2) and more uniform layering structure in the simulated field.

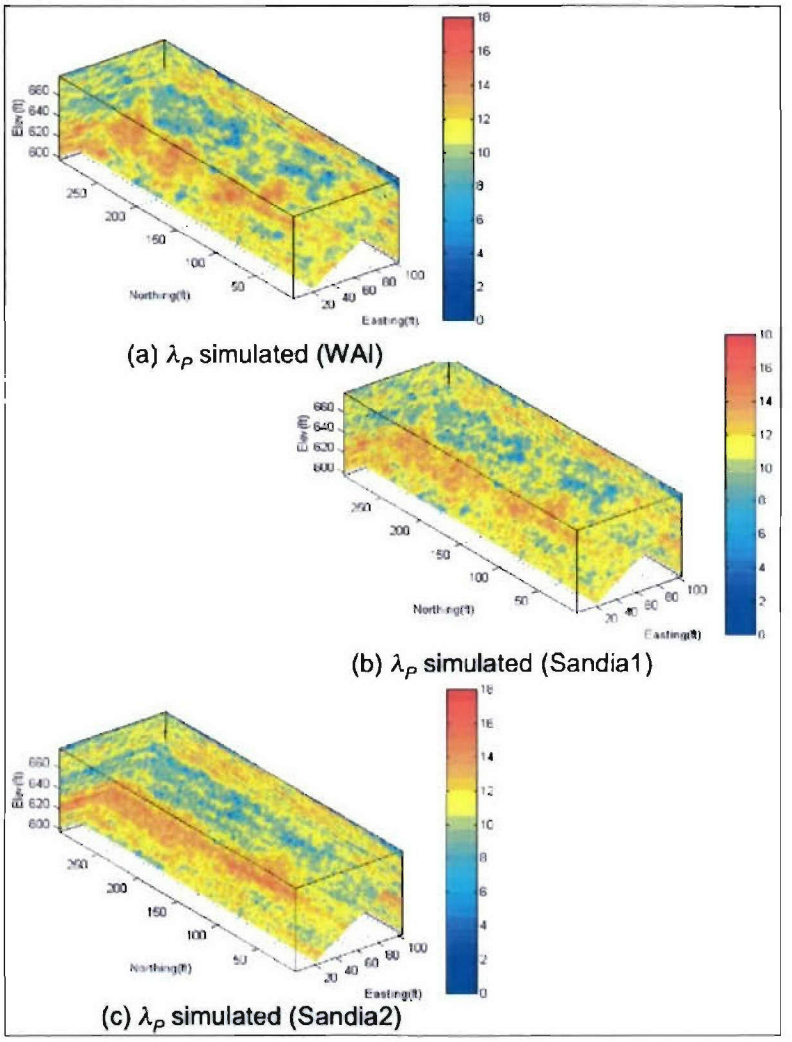

Figure A-2. Comparison of realizations based on the WAI vmodel and the Sandia1 and Sandia2 vmodels given in Figure A-1.